



# Age-depth distribution in western Dronning Maud Land, East Antarctica, from three decades of radar surveys

Steven Franke<sup>1,2</sup>, Daniel Steinhage<sup>2</sup>, Veit Helm<sup>2</sup>, Alexandra M. Zuhr<sup>1</sup>, Julien A. Bodart<sup>3</sup>, Olaf Eisen<sup>2,4</sup>, and Paul Bons<sup>1</sup>

<sup>1</sup>Department of Geosciences, Tübingen University, Tübingen, Germany

<sup>2</sup>Alfred-Wegener-Institut Helmholtz-Zentrum für Polar- und Meeresforschung, Bremerhaven, Germany

<sup>3</sup>Climate and Environmental Physics, Physics Institute and Oeschger Centre for Climate Change Research, University of Bern, Bern, Switzerland

<sup>4</sup>Department of Geosciences, University of Bremen, Bremen, Germany

**Correspondence:** Steven Franke (steven.franke@uni-tuebingen.de)

**Abstract.** Radio-echo sounding provides the opportunity to study the internal architecture of ice sheets through imaging stratified englacial reflections, known as internal reflection horizons (IRHs). They represent consistent time horizons formed at the former ice-sheet surface and buried over time, thus reflecting the ice sheet's age–depth architecture. Their analysis allows crucial insights into past and present boundary conditions, e.g. accumulation rates or basal melting, as well as physical properties and ice dynamics. This study presents a comprehensive data set and insight into the age–depth distribution in western Dronning Maud Land (DML), East Antarctica, spanning the Holocene to the Last Glacial Period (4.8 – 91.0 ka). Using data from various radar systems deployed by the Alfred Wegener Institute between 1996 and 2023, we traced and dated nine IRHs over an area of 450 000 km<sup>2</sup>. A precise age could be assigned to the IRHs by two-way travel time to depth conversion and employing radar forward modelling based on conductivity peaks of the EPICA DML ice core. Six IRHs correlate with past volcanic eruptions. Our findings suggest that most IRHs correspond to IRHs of similar age in other regions of East and West Antarctica, thus likely originating from the same physical reflectors at depth, although they could not be physically connected. This work enhances understanding of the englacial architecture and relationships with snow accumulation and ice-dynamic processes of this sector of the Antarctic ice sheet and provides fundamental data for numerical ice flow models and paleoclimatic studies.

## 1 Introduction

Observing and modelling the Antarctic ice sheet (AIS) is crucial for understanding both past and present climate dynamics and improving projections of future sea-level changes (IPCC, 2023). Deducing its past evolution helps us to comprehend the processes driving ice flow, accumulation, and melting. As one unique observable property, the ice sheet's internal stratigraphy represents a valuable record of past kinematics and dynamics (Siegert et al., 2004; Bons et al., 2016; Leysinger Vieli et al., 2018; Jansen et al., 2024), offering insights into atmosphere–ice–ocean interactions (Drews et al., 2020; Višnjević et al., 2022) and how the ice-sheet system responded to natural climatic variations over a broad range of timescales ranging from hundreds to hundred thousands of years (e.g., Leysinger Vieli et al., 2004; Sutter et al., 2021; Bodart et al., 2023).

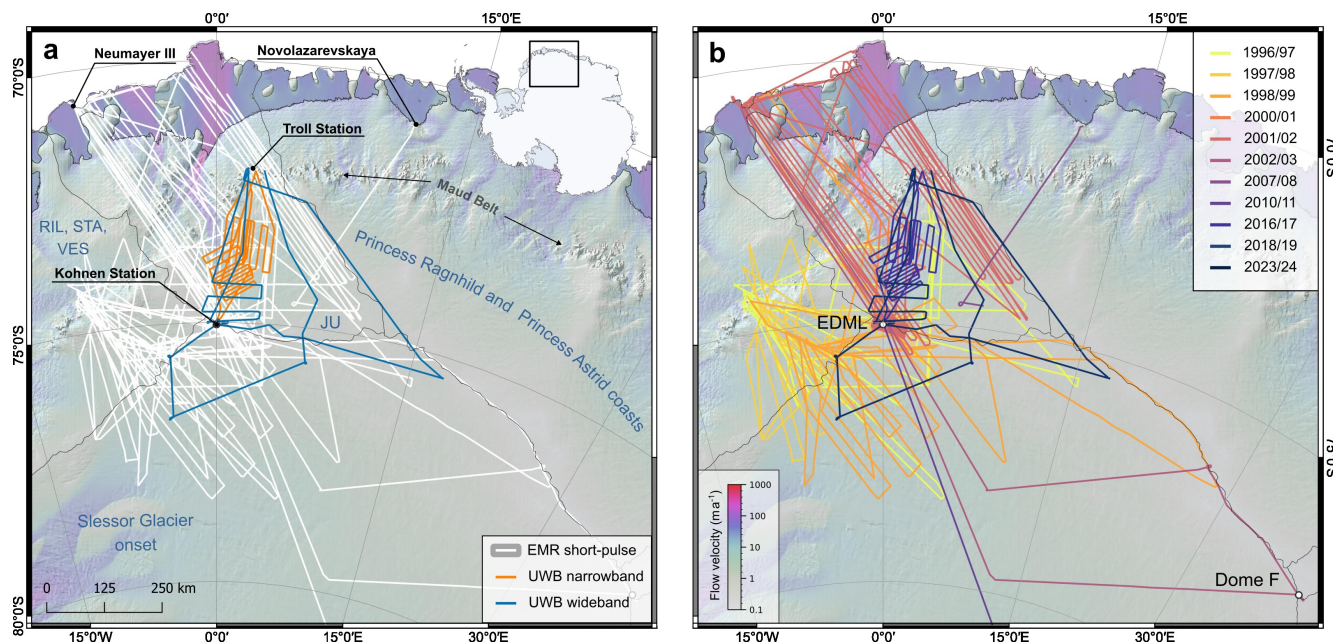


**Figure 1.** Radar profiles used for IRH tracing. (a) Radar profiles are sorted by system: EMR short-pulse (white lines), MCoRDS narrowband (orange lines), and MCoRDS wideband (blue lines). (b) Radar data sorted by acquisition season. Although some profiles extend down to the ice shelf, the IRH tracing region is restricted upstream of the Maud Belt. The drainage basins are marked by thin black lines and are from Zwally et al. (2012).

Radar data provide the opportunity to study the internal architecture of ice sheets (i.e., its stratigraphy) via continuous stratified englacial reflections. These internal reflection horizons (IRHs) occur when radar waves are reflected at boundary layers where the dielectric properties of the ice change (Glen and Paren, 1975; Robin et al., 1977). Dielectric contrasts in ice sheets are primarily caused by variations in density (Robin et al., 1969), electrical conductivity (Paren and Robin, 1975), and changes in the preferred orientation of ice crystals (Harrison, 1973; Fujita et al., 1999). IRHs that are located sufficiently deep below the ice surface, typically within a few hundred meters in Antarctica, are primarily linked to conductivity contrasts and can sometimes be detected across the ice sheet (Millar, 1981; MacGregor et al., 2015; Winter et al., 2019). Strong conductivity contrasts are often linked to deposits of acidic materials from major volcanic eruptions (Hammer, 1980; Millar, 1981). Thus, IRHs represent boundary layers in the ice that indicate time horizons of the same age of snow deposits.

Information about the internal stratigraphy and age–depth architecture of the Antarctic ice sheet is crucial as it serves as a climatic and ice-dynamic record. For instance, it provides insights into past accumulation rates and basal melting, informing us about past surface and basal mass balance (Leysinger Vieli et al., 2004; Eisen et al., 2005; Leysinger Vieli et al., 2011; Cavitte et al., 2018; Bodart et al., 2023; Koch et al., 2023). Since many IRHs can be dated with ice cores, they can also serve as calibration points for ice sheet models (Sutter et al., 2021; Višnjević et al., 2022) and to model basal conditions (Leysinger Vieli et al., 2018; Fudge et al., 2023; Chung et al., 2023; Wang et al., 2023). Additionally, the geometry, depth and continuity



**Table 1.** AWI radar system specifications.

Radar system	Developer	Frequency	Transmit signal	Range resolution	Seasons
EMR	TU HH <sup>a</sup>	150 MHz	60 ns burst	~ 5 m	1996/97, 1997/98, 1998/99 2000/01, 2001/02, 2002/03 2007/08, 2010/11, 2016/17
AWI MCoRDS 5	CReSIS <sup>b</sup>	180–210 MHz (narrowband)	1, 3 & 10 $\mu$ s chirp	4.3 m	2018/19
MCoRDS MCoRDS 5	CReSIS <sup>b</sup>	150–520 MHz (wideband)	1, 3 & 10 $\mu$ s chirp	0.35 m	2023/24

<sup>a</sup> Technical University Hamburg-Haburg

<sup>b</sup> Center for Remote Sensing and Integrated Systems

of IRHs contain information on the cumulative deformation due to ice flow, making them suitable passive markers for ice-dynamic activity and its changes over time, e.g., deciphering folding processes and ice stream activity (Siegert et al., 2004; Bons et al., 2016; Franke et al., 2022a; Jansen et al., 2024), and ice-dynamic processes causing layer discontinuity (Panton and Karlsson, 2015; Sanderson et al., 2023).

The generation and compilation of IRHs using radar data in Antarctica and Greenland remains largely a manual task. While automated methods can successfully trace IRHs to a certain extent (Moqadam and Eisen, 2024), these algorithms often fail to consistently follow the same reflection across multiple intersecting radar profiles and different radar systems, where reflections are depicted differently. Nevertheless, IRHs have been traced and dated across large parts of East Antarctica (Winter et al., 2019; Cavitte et al., 2016, 2021; Wang et al., 2023), West Antarctica (Siegert et al., 2005; Jacobel and Welch, 2005; Ashmore et al., 2020; Bodart et al., 2021; Beem et al., 2021; Muldoon et al., 2018), and Greenland (Karlsson et al., 2013; MacGregor et al., 2015; Franke et al., 2023a). For Antarctica, in particular, these studies have been motivated by the AntArchitecture initiative, a Scientific Committee of Antarctic Research's Action Group which aims to build a 3-D age–depth model of Antarctica from IRHs.

In this study, we present a comprehensive and detailed insight into the dated radiostratigraphy of western Dronning Maud Land (DML; East Antarctica), spanning from the Holocene to the Last Glacial Period, using radar data collected over the past three decades by various recording systems of the Alfred Wegener Institute, Helmholtz Centre for Polar and Marine Research (AWI; Figure 1). Through radar forward modeling based on conductivity data from the EPICA DML (EDML) ice core, we can accurately date IRHs and, in some cases, link them to deposits from past volcanic eruptions. We also discuss the extent to which our dated IRHs can be correlated with those from other Antarctic-wide studies and demonstrate the potential for extrapolating some of these IRHs to much larger areas where an AWI radar system with coarser vertical resolution was used.



## 2 Data and Methods

### 2.1 Radar data

In this study, we utilize three types of radar products that provide sufficiently high range resolution (0.35 – 5 m) and penetration  
60 depth. These radar products were obtained during campaigns conducted by AWI, between 1996 and 2023 with two different  
radar systems.

#### 2.1.1 AWI EMR short-pulse data

The largest pool of radar data is provided by AWI's EMR (Electromagnetic Radar) system, which has been operational in  
Antarctica and Greenland since 1994 (Nixdorf et al., 1999). For IRH tracing, we utilize EMR radar data from nine Antarctic  
65 seasons spanning from 1996/97 to 2016/17 (Figure 1 and Table 1). The EMR system consists of two dipole antennas mounted  
underneath the wings of AWI's Polar Aircrafts (Alfred-Wegener-Institut Helmholtz-Zentrum für Polar- und Meeresforschung,  
2016). The transmission signal is a burst with pulse lengths of 60 or 600 ns at a frequency of 150 MHz, with a pulse repetition  
frequency (PRF) of 20 kHz. For this study, we exclusively utilize EMR 60 ns pulse data (short-pulse data) due to their higher  
70 range resolution to detect IRHs compared to the 600 ns pulse data (see Wang et al., 2023). The short-pulse data have a range  
resolution of approximately 5 m and a vertical sample interval of 13.33 ns. EMR radar data processing comprises filtering and  
along-track stacking with a factor of 7 or 10, which results in a mean trace spacing of ~ 35 and ~ 50 m, respectively (Steinhage  
et al., 2001; Steinhage, 2001; Wang et al., 2023).

EMR survey lines cover the entire western DML (Figure 1). Surveys between 1997 and 1999 focused on the pre-site survey  
of the EDML ice core site (Steinhage et al., 2001; Steinhage, 2001), while surveys between 2001 and 2011 were used to  
75 investigate the internal structure (Eisen et al., 2006, 2007; Drews et al., 2009; Steinhage et al., 2013) as well as ice thickness  
for solid earth geophysical studies in DML (Riedel et al., 2012; Eisermann et al., 2020). The survey in 2016/17 extensively  
surveyed ice thickness at the Dome Fuji ice core site (Karlsson et al., 2018; Wang et al., 2023).

#### 2.1.2 AWI multi-channel chirp data

In addition, we use two data sets acquired with AWI's multi-channel airborne chirp radar system. The system is an improved  
80 version of the Multichannel Coherent Radar Depth Sounder (MCoRDS, version 5; here referred to as AWI MCoRDS system),  
which was developed at the Center for Remote Sensing of Integrated Systems (CREStS) at the University of Kansas (Rodriguez-  
Morales et al., 2013; Hale et al., 2016) and has been in operation since 2016 (Kjær et al., 2018). The radar configuration for  
both campaigns in 2018/19 and 2023/24 consisted of an eight-element antenna array mounted under AWI's Polar 5 or Polar 6  
Basler BT-67 aircraft's fuselage, which serves as transmit and receive antenna array. The transmission signal is composed  
85 of several staged modulated chirp signals, which provide high resolution at different depths (Franke et al., 2022b). Standard  
processing techniques were performed with the OPR Toolbox (Open Polar Radar Toolbox; formerly termed CREStS Toolbox;  
Open Polar Radar, 2023). The main steps include motion compensation, pulse compression, synthetic aperture radar (SAR)





focusing (in the  $fk$  domain) and array processing. Airplane location and orientation is from Global Positioning System (GPS) precise point positioning (PPP) post-processed with a final estimated accuracy (commercial software package Waypoint 8.4) of better than 3 cm for latitude and longitude and better than 10 cm for altitude.

The two AWI MCoRDS campaigns were flown in two different acquisition settings in the 2018/19 and 2023/24 seasons, respectively. In the 2018/19 season, data were acquired with a frequency range between 180–210 MHz (narrowband), which corresponds to a range resolution of 4.3 m. The acquisition settings were optimized to sound deep englacial reflections as well as the bed topography at the onset of Jutulstraumen Glacier (Franke et al., 2021, 2024). MCoRDS data in the 2023/24 season was acquired with a frequency range between 150–520 MHz (wideband), with a range resolution of  $\sim 35$  cm. The acquisition settings were chosen to map near-surface IRHs at high spatial resolution (Koch et al., 2023) in the upstream part of the Jutulstraumen catchment as well as the central plateau South and West of the EDML ice core.

## 2.2 Internal reflection horizon tracing

For tracing IRHs, we utilize the commercial software Emerson Paradigm. To enhance the visibility of isochrones at greater depths, we applied an Automatic Gain Control (AGC) algorithm to the radargrams. IRHs were traced with the following rationale: (1) Existing IRHs, such as the 38 ka and 74 ka isochrones from Winter et al. (2019), were extended, (2) the shallowest and deepest clearly identifiable reflector in the EMR short-pulse data was traced, (3) additional isochrones at regular intervals between those defined in (1) and (2), which are clearly discernible in all radar products.

All isochrones were manually traced with the assistance of a semi-automatic picker, which searches for the maximum within a window width of 5 ns along two picks. An additional gain function was applied to the radar data (also known internally as AGG products) to enhance reflections at all depths. Based on the intersection points of the radar profiles, IRHs were transferred between the different radar products. In cases where the assignment at the intersection point was not clear or the radar reflector was no longer traceable within a profile, no picks were created. We clarify that we use the existing IRHs from Winter et al. (2019) in DML for our representation, dating, and analyses.

## 2.3 Ice base determination

The determination of the ice base reflection for this study is composed of existing and newly traced data. We used existing ice base pick data from the AWI MCoRDS 2018/19 campaign from Franke et al. (2021). Ice base determination from the AWI MCoRDS 2023/2024 season was generated using the OPR Toolbox (Open Polar Radar, 2023) and Emerson Paradigm. For the EMR data, we were able to partially rely on existing data (Steinhage et al., 2001; Riedel et al., 2012), which were either directly traced in the 60 ns short-pulse data or, if flown in toggle mode, traced in the 600 ns long-pulse data and projected to the 60 ns data. For EMR short-pulse profiles used in this study that did not have existing ice base picks, the ice base reflection was traced at locations where IRHs were present and the base reflector was clearly visible.

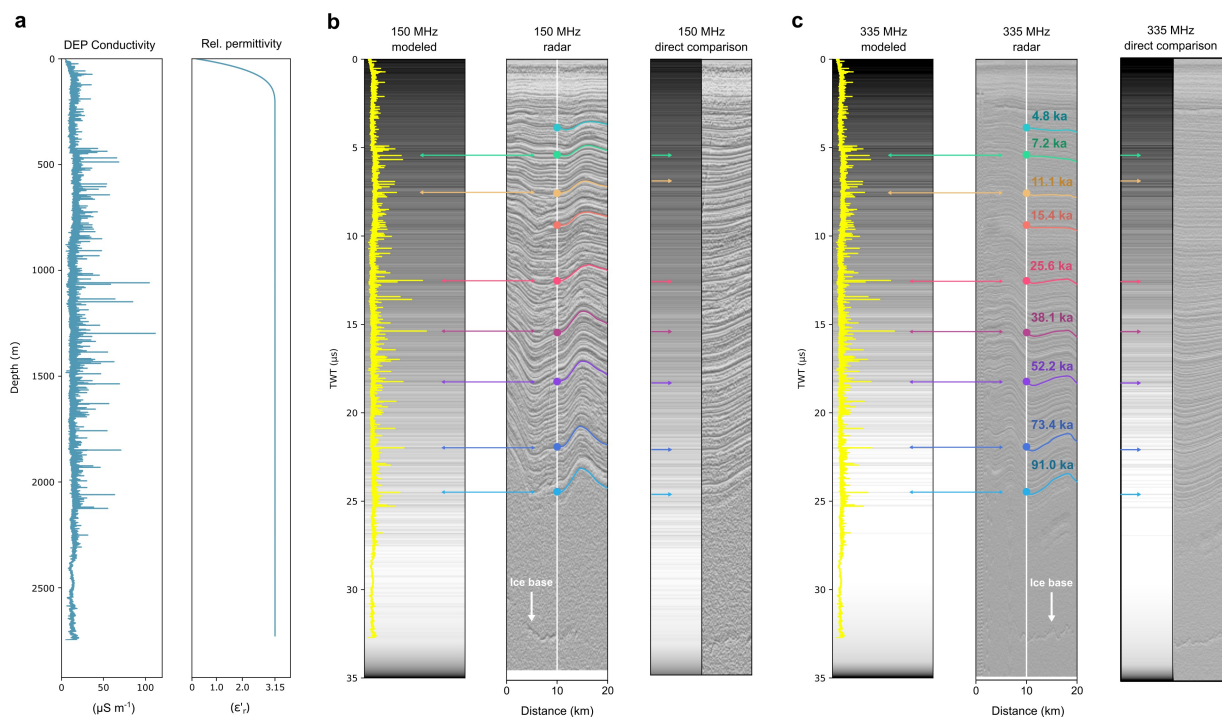


**Figure 2.** Comparison between simulated radar data for 150 and 335 MHz based on measured conductivity at the EDML ice core and radar data collected near EDML. (a) Input parameters for dielectric conductivity and relative permittivity. (b) Comparison between the gprMax simulated radar trace at 150 MHz with overlaid conductivity peaks (yellow) and the EMR profile 20023154 (transmit frequency is 150 MHz). (c) Comparison between the gprMax simulated radar trace at 335 MHz with overlaid conductivity peaks and the MCoRDS wideband profile 20231211\_01\_024 (centre frequency is 335 MHz). The correspondence between simulated reflections, conductivity peaks, and the reflections of our IRHs is marked with coloured arrows. Note that the simulated radargram is the 2D representation of a single trace (without AGC) and the measured radargram has an along-track range of 20 km (with AGC) to enable a better comparison.

## 2.4 Internal reflection horizon dating

To determine the age of the IRHs, we used two different methods: (1) Age dating by converting the IRH radar wave two-way travel time (TWT) from the ice surface to depth and correlating it with the age–depth scale of the EDML ice core (e.g., Cavitte et al., 2016; Bodart et al., 2021), and (2) matching reflections of our IRHs with simulated radar reflections based on conductivity peaks derived from measured DEP (dielectric profiling) data (e.g., Eisen et al., 2003, 2006; Winter et al., 2017). Method (1) has the advantage of allowing the determination of an age for each IRH, albeit with the acceptance of a larger error in depth and age assignment. Method (2) offers greater accuracy and linkage to volcanic events because the conductivity peaks represent the physical origin of reflections (Eisen et al., 2003), however, this approach is not applicable for all IRHs due to some reflections not rising above background noise in the radar data.



**Table 2.** Overview of IRH key characteristics, such as the mean IRH TWT at EDML, mean IRH depth at EDML derived from TWT-to-depth conversion, IRH depths at EDML derived from matching conductivity peaks, IRH ages based on the TWT-to-depth converted depths, IRH ages based on the depth from matched conductivity peaks, and cumulative length of IRHs (line kilometres). The IRH name contains the TWT at EDML in nanoseconds. All TWT-to-depth converted depth values are relative to the ice surface reflection. The conductivity peak depths are from the DEP data set and refer to the depth of the maximum value of the respective conductivity peak.

IRH name	Mean TWT at EDML	Mean depth at EDML	Depth of conductivity peak	TWT-to-depth-based age	Conductivity peak-based age	IRH line-km
IRH_EDML_TWT_3989_ns	3 989 ns	349 m		$4.8 \pm 0.62 \text{ ka}$		28 178 km
IRH_EDML_TWT_5503_ns	5 503 ns	477 m	473.00 m	$7.3 \pm 0.76 \text{ ka}$	$7.2 \pm 0.04 \text{ ka}$	29 555 km
IRH_EDML_TWT_7704_ns	7 704 ns	662 m	650.25 m	$11.2 \pm 0.93 \text{ ka}$	$11.1 \pm 0.03 \text{ ka}^a$	24 846 km
IRH_EDML_TWT_9527_ns	9 527 ns	816 m		$15.4 \pm 1.19 \text{ ka}^b$		13 308 km
IRH_EDML_TWT_12677_ns	12 677 ns	1081 m	1069.72 m	$25.9 \pm 2.08 \text{ ka}$	$25.6 \pm 0.03 \text{ ka}^c$	23 559 km
IRH_EDML_TWT_15661_ns	15 661 ns	1332 m	1311.08 m	$39.0 \pm 2.69 \text{ ka}$	$38.1 \pm 0.02 \text{ ka}^d$	28 238 km
IRH_EDML_TWT_18470_ns	18 470 ns	1569 m	1551.54 m	$53.5 \pm 4.22 \text{ ka}$	$52.2 \pm 0.07 \text{ ka}^e$	19 277 km
IRH_EDML_TWT_22217_ns	22 217 ns	1884 m	1867.55 m	$74.7 \pm 5.34 \text{ ka}$	$73.4 \pm 0.88 \text{ ka}^f$	25 361 km
IRH_EDML_TWT_24723_ns	24 723 ns	2095 m	2080.22 m	$92.4 \pm 7.52 \text{ ka}$	$91.0 \pm 1.10 \text{ ka}$	1 439 km

<sup>a</sup> Large northern hemisphere higher latitude eruption (rank 18 in Lin et al., 2022)

<sup>b</sup> Large lower latitude or southern hemisphere eruption (rank 32 in Lin et al., 2022)

<sup>c</sup> Taupo Oruanui eruption (Dunbar et al., 2017)

<sup>d</sup> Large lower latitude eruption (rank 3 in Lin et al., 2022)

<sup>e</sup> Large bipolar eruption (rank 5 in Lin et al., 2022)

<sup>f</sup> Toba eruption (Svensson et al., 2013)

#### 2.4.1 IRH dating by TWT-to-depth conversion

For the IRH dating using the AICC2023 age–depth scale of the EDML ice core (Bouchet et al., 2023), we used three radar profiles from the seasons 1997/98, 2001/02, and 2023/24, which are located close to the drilling site. Based on the radar traces closest to the ice core for each radar profile (25 m for profile 19983101, 65 m for profile 20023154, and 280 m for profile 20231211\_01\_024), we determined the travel time between the ice surface reflection and the IRHs. For the depth conversion at EDML, we used the constant radar wave speed in ice suggested by Eisen et al. (2006) of  $\sim 1.69 \cdot 10^8 \text{ m s}^{-1}$ , corresponding to a dielectric permittivity of  $\epsilon'_r = 3.145$ . Additionally, we added a value of 13 m to the IRH depths as a firm correction, calculated from measurements of the complex permittivity of shallow firn cores in the region (Steinhage, 2001; Steinhage et al., 2001). To account for the variation in acquisition years and radar products, we averaged the depth values for all three radar profiles. We disregarded the snow accumulation between the recording times of the radar profiles, as the average accumulation rate at



EDML is approximately 5 cm ice equivalent per year, which amounts to about 1.25 m over 25 years and is significantly below the range resolution of 5 m of the EMR system.

For the depth determination error, we included the following parameters: (1) the standard deviation of the depth differences of the respective IRHs from the three radar profiles, (2) the smallest range resolution of 5 m from the EMR system, (3) the span of the tracing window of 5 ns, which corresponds to approximately 0.5 m, and (4) an error in the dielectric permittivity of 1 % (Bohleber et al., 2012). In addition to the age error resulting from the depth error range, the uncertainty of the age in the AICC2023 chronology is also included.

#### 2.4.2 IRH dating by DEP-based radar forward modelling

For age assignment based on simulated radar reflections derived from the measured conductivity of the EDML ice core (Eisen et al., 2006; Winter et al., 2017; Mojtabavi et al., 2022), we used the open-source software gprMax (Giannopoulos, 2005; Warren et al., 2016) to simulate electromagnetic waves in three-dimensional space. This software solves Maxwell's equations using the FDTD method (Taflove and Hagness, 2005) and Yee cells (Yee, 1966), which has proven effective for 1-D and 2-D simulations in ice sheets and glaciers (Franke et al., 2023b; Santin et al., 2023). gprMax uses the same algorithm as already successfully employed for ice-core based forward modelling by Eisen et al. (2006) but includes an efficient solution for model boundary conditions using perfectly matched layers (PMLs; Giannopoulos, 2012) while still offering reasonable computation times for 2-D models. All simulations presented here were performed with gprMax version 3.1.5 (Big Smoke).

For our simulations, we defined a 2-D model domain extending 2.4 m in the x-direction (width) and 2774 m in the z-direction (depth) to represent the full depth of the ice core. To reduce the model size, the y-direction extension was limited to a single cell size, rendering the model 2D to effectively operate in the transverse-electric mode. The cell size in all dimensions is 0.02 m, which enables high resolution, numerical stability, and avoids numerically induced dispersion by ensuring the cell size is at least ten times smaller than the smallest wavelength in our model. Consequently, the time step  $\Delta t$  is 0.047 ns for our cell size. The transmit and receive antennas are placed 1 m below the upper limit of the model domain, in the centre of the x-domain (zero offset). The simulation window for all simulations is 30  $\mu s$ , covering the entire ice thickness at EDML. The antenna represents a Hertzian dipole transmitting a Ricker wavelet polarized in the y-direction. For all simulations, we defined 30 PML cells at the outer boundary of the x- and z-directions.

We conducted simulations using two fixed transmission frequencies: 150, and 335 MHz. These frequencies represent the centre frequencies of the two radar profiles located close to the ice core (150 MHz for the EMR profile, and 335 MHz for the MCoRDS wideband profile). As input data, we used the conductivity measured by dielectric profiling (DEP; Moore, 1993; Wilhelms et al., 1998) along the EDML ice core. We used a constant dielectric permittivity value of  $\epsilon'_r = 3.145$  for the depth range of solid ice. This corresponds to an EM wave propagation velocity of  $\sim 1.69 \cdot 10^8 \text{ m s}^{-1}$ , which is the average value determined by Eisen et al. (2006) at EDML. For the upper  $\sim 180$  m, we fitted a function to the permittivity measured with the DEP until it reached a constant value. The relative magnetic permeability was set to a constant value of  $\mu_r = 1$ , and the magnetic loss factor was set to  $\sigma_* = 0$ .



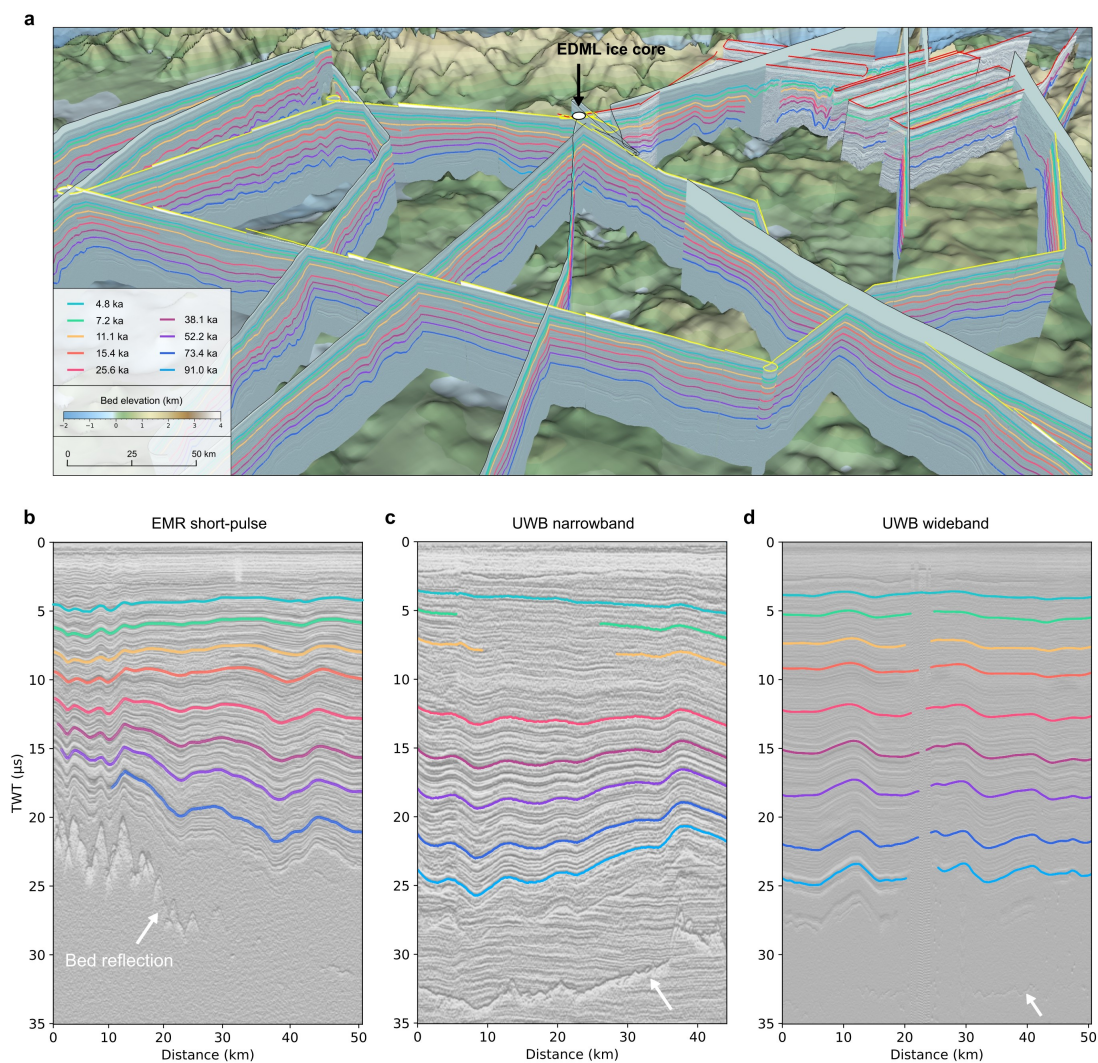


**Figure 3.** Representation of a subset of radargrams (AGC version) of the three different radar products used in this study and traced IRHs in the western DML. (a) Visualization of selected radar data in a 3D canvas with the bed topography (Morlighem et al., 2020) and traced IRHs. Radar profiles with a black line at the top of the fence radargrams are EMR short-pulse profiles, with a red line are narrow bandwidth profiles, and with a yellow line are wide bandwidth profiles. (b) Representation of an EMR short-pulse radargram (profile id: 20023154), (c) a narrow bandwidth radargram (profile id: 20181227\_03\_001), and (d) a wide bandwidth radargram (profile id: 20231211\_01\_024) with IRHs. The radargrams in (b-d) are located close to the EDML ice core and are aligned to the surface reflection.

170 We applied the following signal-processing steps to the simulation output. We derived the reflected energy  $P$  of the synthetic radar data following the methods described by Winter et al. (2017) and Franke et al. (2023b). This involved calculating the envelope of the dielectric field strength (y-component of the electric field,  $E_y$ ) using the Hilbert magnitude transform. Addi-





tionally, the radar trace was smoothed using a 1-D Gaussian filter. This approach enhances the representation of the impulse response of a transmitted radar signal and reflections from a smooth reflector. The final signal strength was obtained by converting the electric field envelope to decibel (dB) ( $20 \log_{10}(Ey)$ ). We did not apply corrections for geometric spreading or  
175 englacial attenuation.

For the age assignment, we examined which of the simulated reflections originated from conductivity peaks and matched the IRHs (Eisen et al., 2006). We then determined the depth of the corresponding conductivity peaks (if present and unambiguous to determine), and used this depth to assign the age via the AICC2023 age–depth chronology (Bouchet et al., 2023). This method  
180 is less dependent on the choice of radar wave propagation velocity in ice, firm correction factor, and ice surface determination, relying solely on the assignment of conductivity peaks, and provides a clearer age determination with a smaller associated error. Hence, for the error estimation, we only consider the dating error provided in the AICC2023 age–depth chronology. In addition, it can be used to better estimate the average relative permittivity of the ice at the ice core site.

## 2.5 IRH depth and normalized depth

185 We derived the depth of all IRH points by calculating the TWT between the ice surface and the IRH. Then, we converted the TWT to depth using (e.g., Steinhage et al., 2001; MacGregor et al., 2015; Cavitte et al., 2016; Winter et al., 2017; Ashmore et al., 2020; Bodart et al., 2021):

$$Z_{irh} = \frac{TWT C_{air}}{2 \sqrt{\epsilon_r'}} + Z_{firm}, \quad (1)$$

where  $C_{air}$  is the electromagnetic wave speed in air ( $C_{air} = 2.9971 \cdot 10^8 \text{ m s}^{-1}$ ). For the calculation of IRH depths, we use  
190 a constant dielectric permittivity of  $\epsilon_r' = 3.15$ . This value deviates slightly from the empirically determined value at EDML (Eisen et al., 2006), but it is a realistic estimate for the spatial extrapolation within our study area. Additionally, we apply a firm correction of 13 m (Steinhage, 2001), which is the best-known value in this region.

Additionally, we calculated the normalized depth of the IRHs within the ice column, which provides a better comparison to determine whether IRHs lie deeper or shallower within the ice column in specific areas. We divided the IRH depth below  
195 the ice surface by the ice thickness. Here, we only use ice thickness values at locations where ice base picks are available, as differences in ice thickness compared to gridded products like BedMachine (Morlighem et al., 2020) can result in significant discrepancies, which can strongly influence the relative position of IRHs within the ice column. These discrepancies are due to interpolation methods and the fact that not all ice thickness data used here are yet included in BedMachine.

## 2.6 Data validation

200 We validated our traced IRHs using a crosspoint analysis for each IRH. To achieve this, we calculated crossover points along the traced horizons and determined the depth difference between two intersecting IRHs (see Appendix A for details). This ensured that the same IRHs were traced across intersecting transects across our study area. In total, we analysed more than 2000 crossover points and the differences for all IRHs in the crossover analysis range between 0 and 74 m, with a mean

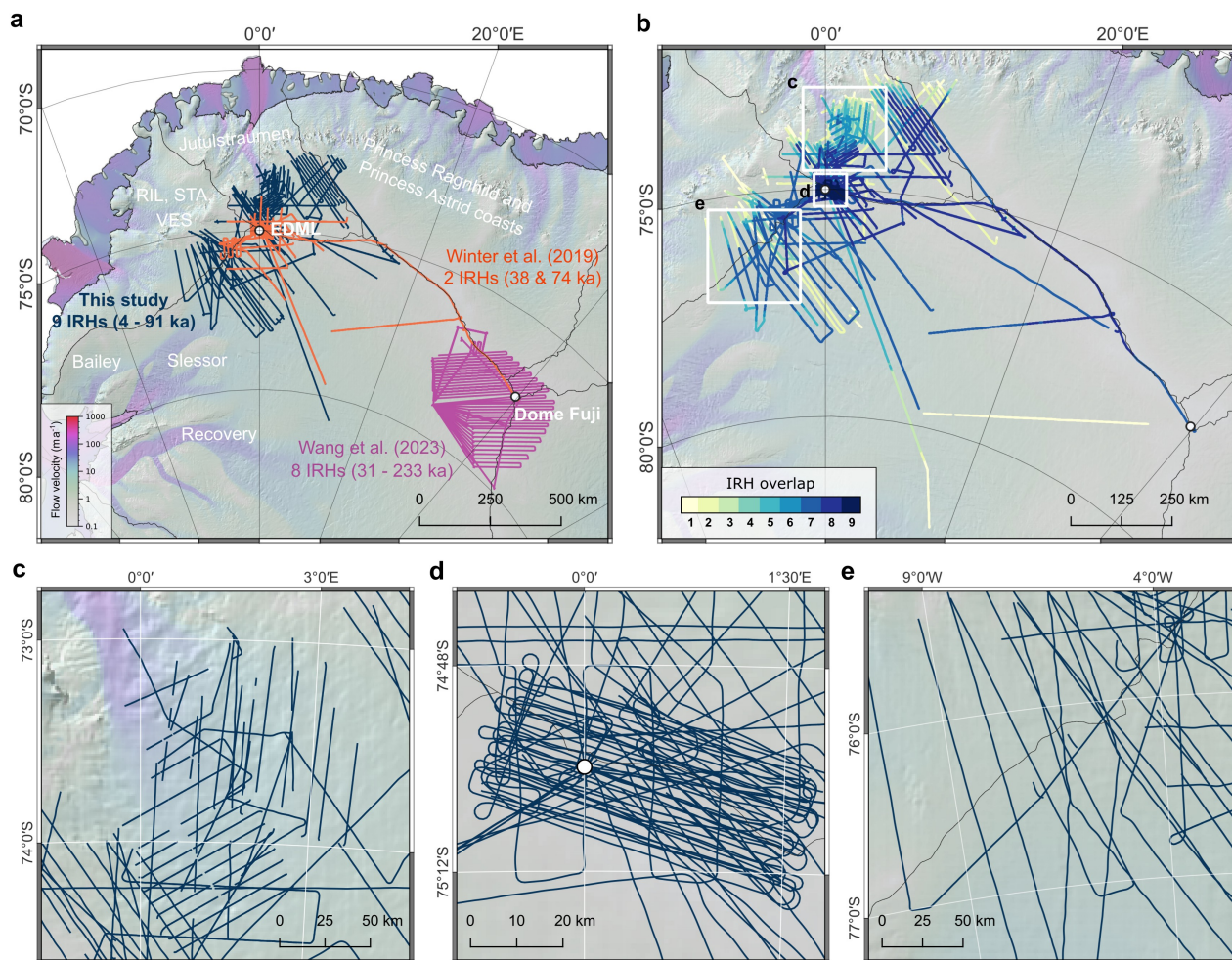


**Figure 4.** Location, vertical overlap, and spatial distribution of IRHs. (a) Spatial distribution of IRHs from this study (dark blue) in DML and of IRHs from other studies in this region (Winter et al., 2019; Wang et al., 2023, orange and purple, respectively). (b) Color-coded overlap of IRHs. (c–e) Magnified views showing the spatial coverage of IRHs in key regions: (c) Jutulstraumen Glacier onset, (d) EDML ice core site and (e) ice divide south-west of EDML (locations indicated by white boxes in panel b).

standard deviation of 3.75 m. Since we traced the ice surface at the highest gradient of surface return power, while the IRHs  
 205 were traced at their maximum return power, a certain fluctuation in depth at the crosspoints is expected. The individual results  
 of the crosspoint analysis and details on the method are presented in Appendix A.



### 3 Results

#### 3.1 IRHs ages in EMR short-pulse and MCoRDS data

Two different dating methods provided IRH ages ranging from 4.8 to 91.0 ka (Table 2) covering the Holocene and Last Glacial  
210 Period. We use the age derived from the depth of conductivity peaks to date the IRHs due to their greater accuracy and only use  
the age from TWT-depth conversion in the radar profiles when no conductivity peak could be assigned. The radar reflections  
of seven of nine IRHs could be clearly associated with conductivity peaks in the EDML core using radar forward modelling  
(Fig. 2).

#### 3.2 Spatial extent of IRHs in DML

215 The overall coverage of traceable IRHs in this study spans the entire western DML, covering an area of approximately  
450 000 km<sup>2</sup>. IRHs extend over 700 km south of the EDML ice core, ~200 km north and ~400 km south-west and north-  
east. IRHs also extend along the divide between EDML and Dome Fuji ice core sites into a region where IRHs were traced  
extensively in AWI's EMR long-pulse data (Fig. 4 a; Wang et al., 2023). The horizontal density of traced IRHs varies signifi-  
cantly (Fig. 4 c–e) and is highest within a radius of about 30 km around the EDML ice core (Fig. 4 d). Additionally, there  
220 is dense coverage in the Jutulstraumen drainage basin south of the Maud Belt, particularly at the onset of the Jutulstraumen  
Ice Stream (Fig. 4 c). Furthermore, there is a high density of IRHs southwest of the EDML ice core at the divide between the  
Slessor, Bailey, and Recovery drainage basins and the Riiser-Larsen, Brunt drainage basin (Fig. 4 e). Generally, IRHs cover  
mostly slow-moving regions, in particular at the ice divides. Regions of higher flow velocities are covered at the onset of  
Slessor ice stream (~35 m yr<sup>-1</sup>) and Jutulstraumen Glacier (<100 m yr<sup>-1</sup>).

225 IRHs could be consistently traced in most radar profiles. However, there are gaps, particularly in the area of the Jutulstraumen  
Ice Stream, which increase downstream as the internal layers become more folded due to ice flow convergence and the deep  
canyon system (Franke et al., 2021). Strongly dipping internal layers show a loss in return power depending on their dip angle  
at depth due to off-nadir ray path losses and destructive interference (Holschuh et al., 2014). Moreover, gaps in the 4.8 and  
sometimes in the 7.2 ka IRH occur because the surface multiple reflection overlays these IRHs, which makes continuous tracing  
230 difficult.

The IRH overlap is greatest in the vicinity of the EDML ice core, where all nine IRHs could be traced nearly continuously.  
Here, the layer continuity is least disturbed by ice flow and both shallow and deep IRHs are well-resolved in all radar systems.  
There is also high IRH overlap at the onset of the Jutulstraumen Ice Stream and along the ice divide towards Dome Fuji. The  
lowest overlap is generally found in the part of radar profiles closest to the Maud Belt, where deeper and older IRHs become  
235 absent.

In our region, IRHs with ages of 38.1 ka and 73.4 ka were previously traced and published by Winter et al. (2019). This IRH  
archive is now significantly expanded by several hundreds of kilometres around EDML. The 38.1 ka and 73.4 ka horizons are  
extended by ~450 % and ~480 %, respectively. Additionally, seven more IRHs were added with comparable coverage (Figure



4 b). Based on the existing dataset of IRHs from (Winter et al., 2019), this represents a total increase in IRH data points by  
240 ~ 1860 %.

### 3.3 Spatial variation in IRH depth distribution

Our IRHs, that range between 4.8 and 91.0 ka in age, are found at depths between 200 and 2200 meters below the ice surface (Figure 5). Both the absolute depth below the ice surface and normalized depth distribution of the IRHs show significant variation. We observe a general pattern where IRHs around the ice divide near EDML and to the west are deeper compared  
245 to IRHs further south and towards Dome Fuji (Figure 5 and 6). This pattern is even more pronounced in the normalized IRH depths along the ice divide between EDML and Dome Fuji. Additionally, we note a contrasting trend when comparing absolute and relative IRH depths at the edges of the Maud Belt and on the plateau. For the 73.4 ka IRH, for example, it is evident that northeast of EDML, this IRH lies at depths of approximately 1000 to 1200 meters, similar to the southeastern part near Dome Fuji (comparison of Feature A and Feature B in Figure 5). However, the relative depth reveals that the 73.4 ka IRH is about  
250 65 % below the surface northeast of EDML, but only about 45 % near Dome Fuji. This pattern is also evident in the 11.1 ka, 25.6 ka and 38.1 ka IRHs, however with smaller differences as the IRHs become younger (comparison of Feature A and Feature B in Figure 6).

The IRH depths within the Jutulstraumen drainage basin are particularly variable and show the following pattern in their relative depths: In the southwestern part of the Jutulstraumen onset region, the IRHs are significantly deeper (absolute depth)  
255 than in the northeastern area. The IRHs in this region (denoted as Feature A in Figures 5 and 6) are significantly shallower compared to the southwest and east but show similar relative depths to EDML. This general pattern is evident in all IRHs that cover this region. A different pattern emerges when considering absolute depths. We find a greater variation with very shallow IRHs in the northeast and very deep IRHs in the Jutulstraumen Trough area. In the 38.1 ka IRH, these depth differences amount to up to 1500 m.

260 Additionally, the variation in depth of the IRHs is striking in two profiles extending from EDML towards the south-southeast. Around 79.9° S, there is a significant increase in absolute depth followed by a decrease to more shallow depths, observable in all IRHs from 7.2 ka onward (Feature C in Figure 5). This pattern is more pronounced in older IRHs compared to younger IRHs. However, there is no information on the relative IRH depth at this location since the ice base reflection is not visible in this section of the radar profile. Moreover, we observe an increase in absolute IRH depth at the southwestern edge of our IRH  
265 data, which is particularly pronounced in the 25.6 and ka and 38.1 ka IRHs (Feature D in Figure 5). Notably, older IRHs of this particular region could not be traced in the radar data.



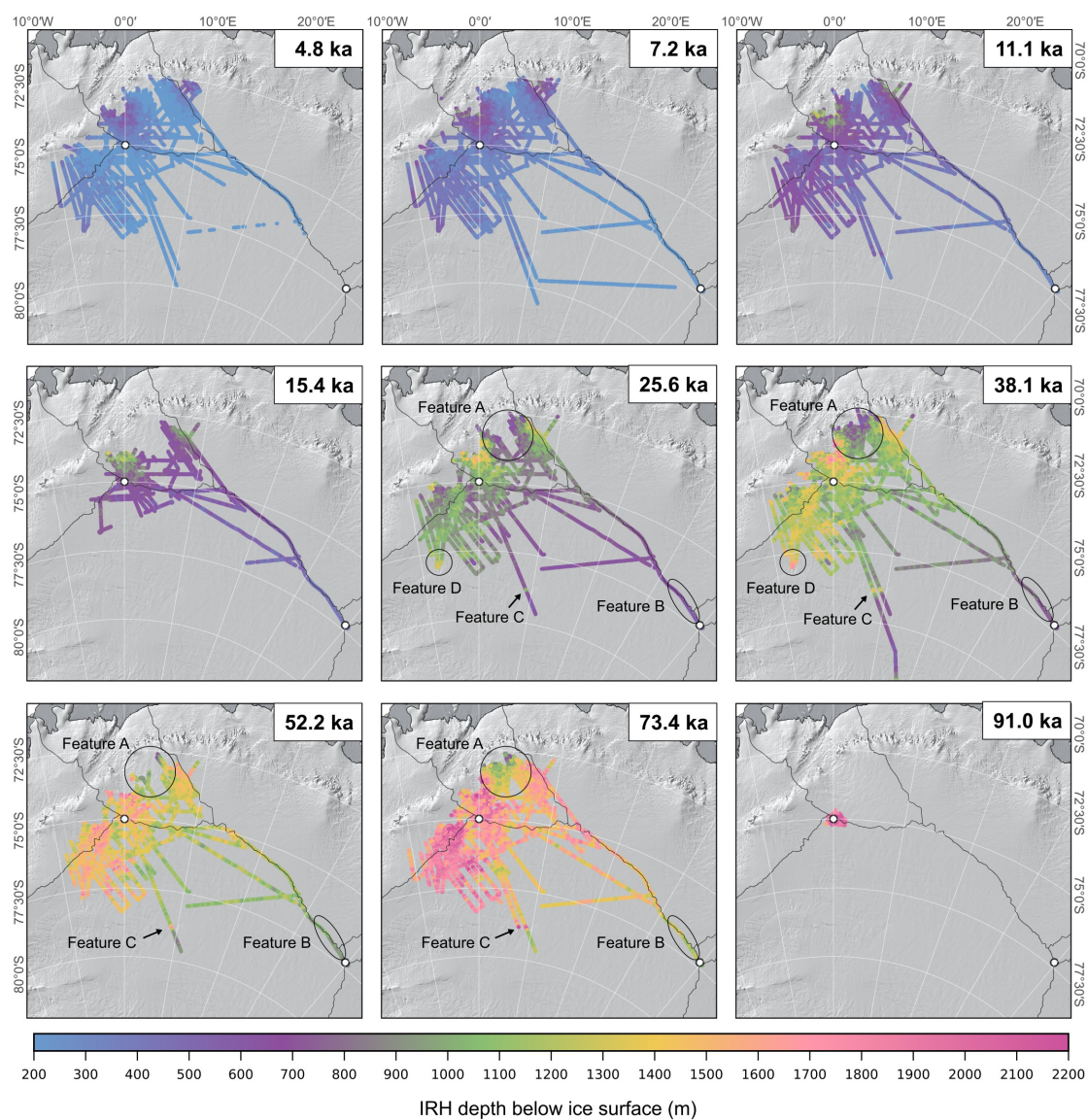


**Figure 5.** Color-coded absolute depth representation of the nine IRHs from this study. The background map displays the ice surface elevation REMA (Howat et al., 2019) in hillshade. The fine black lines delineate the drainage basins according to Zwally et al. (2012).



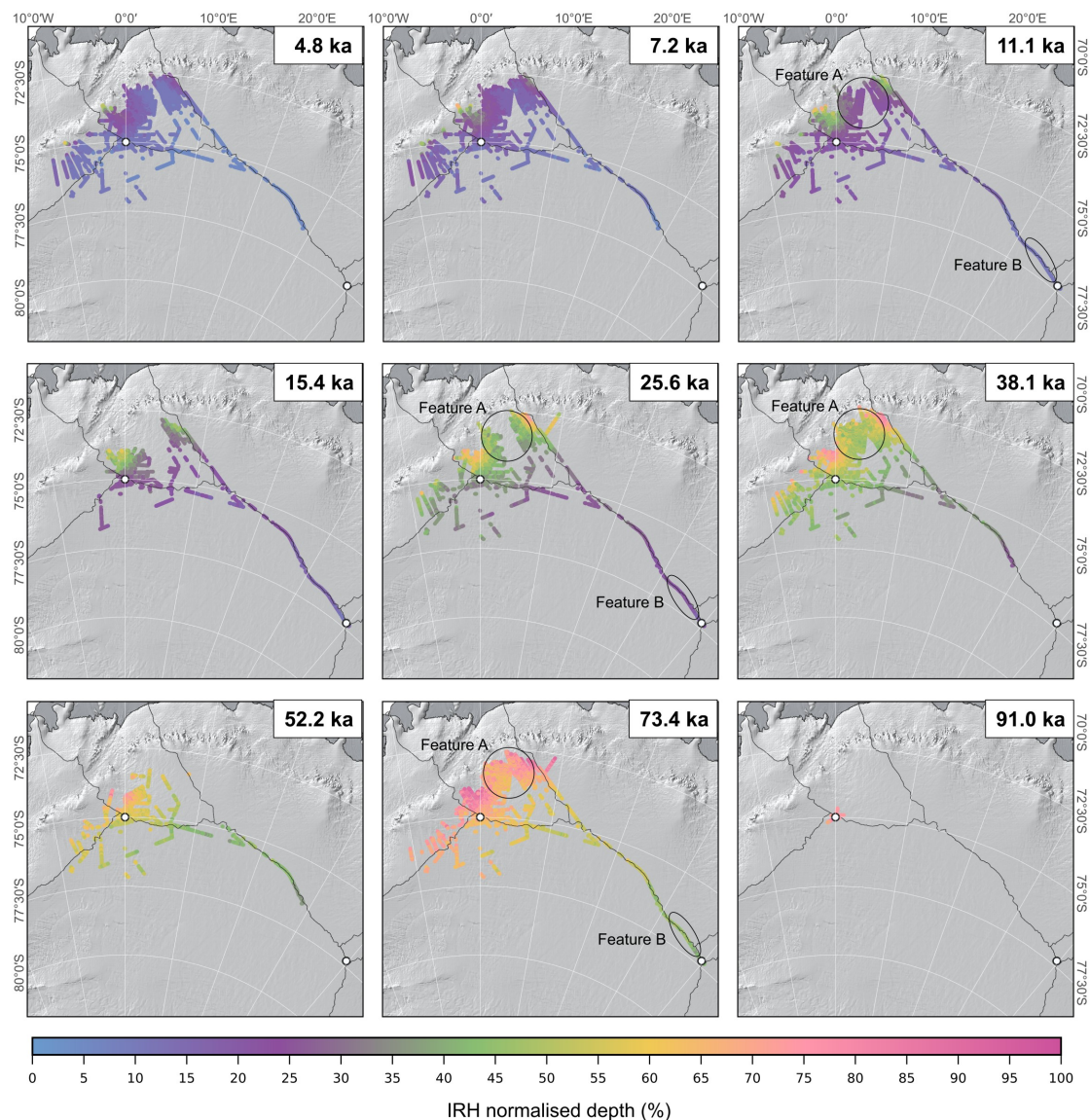


**Figure 6.** Color-coded normalized depth representation of the nine IRHs from this study. The background map displays the ice surface elevation REMA (Howat et al., 2019) in hillshade. The fine black lines delineate the drainage basins according to Zwally et al. (2012).

## 4 Discussion

### 4.1 Interpretation of IRH depth distribution variations

Feature A (Figures 5 and 6) represents a notable anomaly in a region characterized by particularly shallow IRHs in both  
270 absolute and relative depths. This region deviates from the general trend of having a gradient from shallower IRHs on the

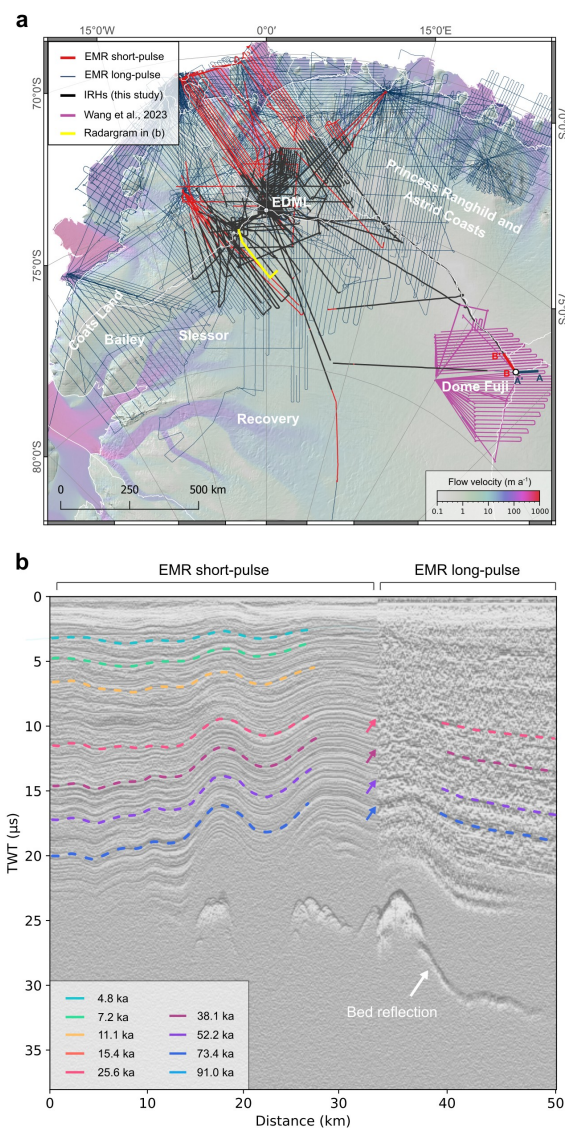


**Figure 7.** Potential to extrapolate IRHs to AWI EMR long-pulse data. (a) Overview of EMR short-pulse data (red) superimposed with the IRHs traced in this study (black), and in the background showing the EMR long-pulse data (dark blue). The IRHs from Wang et al. (2023) are depicted in purple. The lines A – A’ (black) and B – B’ (red) in a) indicate a long-pulse and short-pulse radargram at Dome Fuji (Figure B1) where IRHs from this study and IRHs from Wang et al. (2023) intersect. (b) Composite radargram (AGC version) from EMR short-pulse and long-pulse data (profile ID 19992116, long-pulse, right; 19993116, short-pulse, left). At the intersection, transitions where IRHs from this study are also represented in the long-pulse data are marked with arrows.

plateau to deeper IRHs (especially in relative depth) near the Maud Belt. This general trend is likely linked to the overall snow accumulation pattern, with higher accumulation rate towards the Antarctic coast and lower accumulation rate on the



plateau. The shallow IRHs in Feature A are likely also accumulation-driven, as this area shows significantly reduced snow accumulation, as determined from firn core analysis (Rotschky et al., 2007). The fact that this pattern is also evident in older IRHs suggests that this low-accumulation anomaly may have persisted in this region not only during the Holocene but also during the Last Glacial Period, given that the ice in this region shows very low flow velocities.

Additionally, IRHs are particularly deep (both absolute and relative) in the southwestern area of the Jutulstraumen onset, which could be linked to the ice stream activity. Besides dynamic thinning, increased friction at the ice base could lead to basal melting, causing the IRHs to subside both absolutely and relatively. However, our work also shows that ice older than 73.4 ka is present in the main trunk of Jutulstraumen, at least at its onset. Further northeast, the shallow depths of the IRHs might be explained not only by the low-accumulation anomaly but also by reduced basal sliding, less basal melting, and even a positive basal mass balance due to basal freeze-on on subglacial water (Franke et al., 2021, 2024).

A comparison of IRH depths between Feature A (south of the Maud Belt) and Feature B (near Dome Fuji) highlights the importance of considering the relative depth of IRHs in relation to ice thickness. The fact that all IRHs traced near Dome Fuji are significantly shallower relative to ice thickness than those further northwest can be explained by the ice sheet's geometry and surface mass balance. Both regions are characterized by low accumulation rates (Rotschky et al., 2007; Oyabu et al., 2023), but the ice at Dome Fuji is overall much thicker and significantly older at greater depths compared to further north. This results in lower relative depths for the IRHs.

The sudden IRH depth increase of all ages along the southward-trending radar profiles (Feature C) and some IRHs in the southwest (Feature D) could be explained by changes in bed elevation. Although there are no visible bed reflections in the radar profiles where the IRHs were traced, ice thickness data from nearby regions suggest a connection with the underlying topography. The bed topography data from BedMachine (Morlighem et al., 2020) indicate that the IRH depth increase in Feature C is associated with a subglacial valley with a width between 15–25 km. The IRHs at Feature D are located at the onset of one of the tributaries of the Slessor Ice Stream. Higher flow velocity at this point would dynamically thin the ice, which must be compensated by lateral mass influx or increased snow accumulation, which would increase IRH depths. Hence, the relative drop of the IRHs in this area could indicate the long-term activity of this tributary. The fact that older IRHs, such as the 52.2 ka and 73.4 ka reflector, could not be traced in this area further supports the hypothesis of a significant dynamic component causing IRH subsidence or layer disruption, which could suggest that this ice stream system has been stable at least for the past ~ 70 ka.

#### 4.2 Link between IRHs and volcanic eruptions

The dominant origin of IRHs was attributed to changes in conductivity due to variations in acidity originating from deposits of large volcanic events (Millar, 1981). Six of the IRHs that we dated using conductivity peaks and one depth-based IRH can be associated with major bipolar volcanic eruptions during the Holocene and Last Glacial Period (Lin et al., 2022; Svensson et al., 2013). Our 11.1 ka IRH, associated with a moderate conductivity peak, can be correlated with the deposits of a bipolar eruption event dated to 11.3 ka BP. These deposits have been identified in both Antarctic and Greenland ice cores (Lin et al., 2022). Additionally, we consider the possibility that our 15.4 ka IRH could be linked to an event dated to 15.6 ka BP. Although



there is no clear and strong conductivity peak in the EDML ice core for this event, one explanation could be that this event is classified as a relatively weaker bipolar eruption compared to others (rank 32; Lin et al., 2022).

The radar reflection of the 25.6 ka IRH can be linked to sulfate deposits from the New Zealand Taupo, Oruanui eruption, 25.32 ka BP, which were detected in two Greenland (undetected in GISP2) and three Antarctic ice cores (Lin et al., 2022) and confirmed by tephra deposits in Antarctica (Dunbar et al., 2017). The IRH we dated to 38.1 ka is very likely associated with the third strongest bipolar eruption in the Last Glacial Period known to date, which occurred at 38.13 ka BP. The exact eruption location is unknown, but it is likely a low-latitude or Southern Hemisphere eruption with an estimated average climate forcing twice as strong as the Tambora eruption in 1815 CE (Lin et al., 2022). Our 52.2 ka IRH could correspond to an eruption that occurred at 52.2 ka BP and is listed as the fifth strongest eruption in Lin et al. (2022). The deposits from this eruption can be traced in three Greenland and three Antarctic ice cores (Lin et al., 2022), and the possible eruption site is estimated to be in the high-latitude Northern Hemisphere (above 40° N).

From tracing IRHs in the radar data in this region, we find that the reflection of the 73.4 ka IRH is the most discernible and extensive in the deeper third of the ice sheet. As per Winter et al. (2019), we also speculate that this reflection most likely corresponds to the deposits of the Toba eruption in northwest Indonesia, dated using tephra and Ar-Ar dating to  $73.88 \pm 0.32$  ka BP and  $75.0 \pm 0.9$  ka BP, depending on the location of the deposits (see references in Svensson et al., 2013). The Toba eruption is considered the largest known supereruption of the last 2.5 million years (Chesner, 2012) and likely occurred during the cooling transition from Greenland Interstadial 20 to Greenland Stadial 20 (Lin et al., 2023, and references therein).

### 4.3 Comparison with IRHs from other studies

Steinhage et al. (2013) traced eight IRHs along the ice divide connecting EMR short-pulse profiles between EDML and Dome Fuji and dated them via TWT-to-depth conversion using the EDML AICC2012 age–depth chronology (Bazin et al., 2013). Several of these isochrones correspond with those we have traced over a much larger spatial extent in this study (corresponding IRH ages dated at the EDML core by Steinhage et al., 2013, shown in parentheses): 4.8 ka (4.7 ka), 7.2 ka (7.4 ka), 25.6 ka (25.1 ka), 38.1 ka (38.1 ka), and 73.4 ka (72.4 ka). The discrepancies arise due to a combination of the choice of radar profiles, different dating methods, the type of surface pick, and the selected propagation speed for radar waves in ice, all of which are within the stated error margins. Additionally, the IRHs in Steinhage et al. (2013) were also dated using the Dome Fuji age–depth chronology, resulting in different ages. Moreover, the 38.1 ka and 73.4 ka IRHs were already traced to a large extent in our study area by Winter et al. (2019). These data provide an essential foundation for this study, as they seamlessly connect with our dataset. Winter et al. (2019) also mention that IRHs with ages of 4.8, 7.6, 15.4, and 25.0 ka were traced to a smaller extent (and very likely correspond to the same IRHs in our study), but were not published.

A comparison with traced IRHs in East Antarctica, in the region of the Vostok ice core and EPICA Dome C ice core (Leysinger Vieli et al., 2011; Cavitte et al., 2016, 2021; Winter et al., 2019) suggests that some of these IRHs likely correspond to those identified in our study. Most of these isochrones extend far beyond an age of 100 ka, reaching up to approximately 700 ka, with the dating of the oldest IRHs being particularly challenging due to the inherent uncertainties associated with the 1-D age-depth model used to date (Cavitte et al., 2021). The 38.1 ka and 73.4 ka IRHs (dated to the same ages by Cavitte





et al., 2021), are almost certainly the same reflections in this region, as they exhibit overall very strong reflections in our survey area and correlate with significant past volcanic eruptions (Lin et al., 2022; Svensson et al., 2013). Furthermore, our isochrones extend into the area around Dome Fuji, for which there are dated IRHs from Wang et al. (2023). However, these were traced using EMR long-pulse data, which have a vertical resolution of  $\sim 50$  m, making the direct comparison more difficult. 345 Nonetheless, they also identified IRHs dated to  $36.3 \pm 3.6$  ka and  $75.3 \pm 7.0$  ka, which, when examined at the intersection points with our EMR short-pulse radar data, most likely represent the same englacial reflectors (see Appendix B).

Dated IRHs with similar ages to ours are not confined to East Antarctica. Several studies have traced, dated, and published IRHs in West Antarctica (Muldoon et al., 2018; Ashmore et al., 2020; Beem et al., 2021; Bodart et al., 2021, 2023). Notably, in particular, our 4.8 ka IRH appears to be widespread in West Antarctica. For instance, Muldoon et al. (2018) identified a 4.7 ka 350 IRH across West Antarctica's ice divide and throughout the Thwaites Glacier catchment, Beem et al. (2021) traced a 4.7 ka IRH at Titan Dome, and Bodart et al. (2021, 2023) identified a 4.72 ka IRH across the divide and throughout the Pine Island Glacier catchment, with direct links showing vertical conformity with another IRH widely traced across the Institute and Möller Ice Stream Catchment by Ashmore et al. (2020). Additionally, there may be further links between our 7.2 ka IRH and the 6.94 ka 355 and our 11.1 ka and 73.4 ka IRHs and the 10.7 ka and 72.5 ka IRHs from Beem et al. (2021). However, to accurately determine if these dated isochrones indeed originate from the same reflector Antarctic-wide, it would be necessary to link not only the IRH ages (which can vary depending on the ice core, method, and determined TWT between the ice surface and the IRH) but also the backscatter patterns in the radar data. Here, radar lines connecting datasets between East and West Antarctica would be beneficial. However, this presents challenges, such as long flights over the Antarctic plateau, and geographical difficulties, 360 such as the loss of layer continuity across the Transantarctic Mountains. For a definitive connection of IRHs that relate to the same reflectors and, therefore, the same deposits, geochemical analyses of ice cores could provide additional constraints.

In the future, the AntArchitecture initiative will aim to compile all such IRH datasets into a continent-wide radiostratigraphic database, which will be used to create a three-dimensional age–depth model of the ice sheet by interpolating between known IRH along-track datasets similar to already existing gridded topographic models such as Bedmap (Lythe and Vaughan, 2001; 365 Fretwell et al., 2013; Frémand et al., 2022) and BedMachine Antarctica (Morlighem et al., 2020). For such a task to be successful, additional IRH tracing will need to take place in poorly surveyed areas of the ice sheet or away from ice divides and ice-core locations using existing RES coverage to avoid over-fitting the interpolation algorithms. By utilizing three decades of RES data from multiple radar systems in the area, this study bridges a significant gap in the East Antarctic radiostratigraphic record and thus in our ability to obtain a continent-wide age–depth model of the ice sheet, as envisaged by AntArchitecture.

#### 370 4.4 Potential to expand IRH coverage in western DML

In our study, we have not fully utilized the complete archive of AWI radar data. We focused on EMR short-pulse, MCoRDS narrow and MCoRDS wide bandwidth data because these have similar vertical resolutions (5 m or better), enabling the capture of a higher number of IRHs that are comparably represented across these systems. However, there are additional areas in DML covered exclusively by EMR long-pulse data (approximately 50 m vertical resolution but deep-sounding). At intersections





375 between EMR short-pulse and long-pulse data where we were able to trace IRHs, it becomes apparent that the 25.6, 38.1,  
52.2, and 73.4 ka IRHs are also represented in the long-pulse data (Fig. 7 b), which aligns with the IRHs of similar age in  
Wang et al. (2023). The representation of the same reflectors in EMR long-pulse and short-pulse data does not only account  
for reflections caused by changes in electrical conductivity but also for reflections caused by changes in ice crystal lattice  
orientation (Eisen et al., 2007). Considering the AWI EMR radar line coverage in Figure 7 a, there is additional potential,  
380 particularly for regions upstream of Princess Ragnhild and Princess Astrid coasts, as well as the onsets of the Slessor and  
Recovery ice streams. Additionally, the spatial coverage of the East Antarctic plateau between EDML and Dome Fuji could be  
significantly improved. It may even be possible to establish connections between our IRHs and the western Coats Land at the  
ice divide to the Bailey and Slessor basins using AWI's and the British Antarctic Survey's radar data (Frémand et al., 2022),  
which are of similar range resolution.

#### 385 4.5 Significance of dated IRHs for reconstructing the ice-sheet history in western DML

Reconstructing past ice sheet configurations is crucial for understanding ice-sheet processes and their impacts on the Earth  
system, as well as providing essential constraints for ice sheet models. The spatial depth distribution of our nine IRHs in western  
DML can significantly contribute to understanding ice-sheet evolution. By comparing IRH depths and spatial anomalies, we  
can test hypotheses about underlying mechanisms, such as surface or basal mass balance and ice-dynamic processes, and how  
they may have changed over time. Our dated IRHs also provide an opportunity to validate or expand existing findings and  
390 hypotheses on ice surface changes based on cosmogenic nuclides (Andersen et al., 2020) about past ice dynamics in DML  
(Andersen et al., 2023; Braga et al., 2023). In addition, the absolute and relative depth of our IRHs offer the opportunity to  
complement studies on e.g., preserved paleo-geomorphological structures (e.g., Näslund, 1997; Rose et al., 2015; Franke et al.,  
2021; Carter et al., 2024) or regions of basal freeze-on of subglacial water (e.g., Bell et al., 2011; Leysinger Vieli et al., 2018;  
395 Franke et al., 2024) providing further insights into past flow behaviour and ice sheet configurations.

Furthermore, we see significant potential for improving regional and Antarctic-wide ice sheet models to provide better  
projections for future sea-level rise (Sutter et al., 2021). Our IRHs can serve as a crucial tool for calibrating results in model  
simulations (Sutter et al., 2021; Višnjević et al., 2022). Especially in dynamic regions such as the Slessor and Jutulstraumen  
ice stream onset regions, our IRHs are particularly valuable for testing hypotheses of their stability over multiple glacial cycles  
400 (Rippin et al., 2003, 2006). Conversely, IRH data from less dynamically active regions, such as the ice divide south-west from  
EDML, along the divide between EDML and Dome Fuji, the region south of EDML, as well as the shallow-IRH anomaly region  
(Feature A), are well-suited for inferring the spatial distribution of past accumulation rates (Eisen et al., 2005; Huybrechts et al.,  
2009; Leysinger Vieli et al., 2011).

An additional approach to decipher the past ice dynamics of a region using IRHs lies in the structural analysis of three-  
405 dimensional englacial structures, particularly the geometries of folds, fold axial planes, and the development of fold amplitudes  
with depth (Bons et al., 2016; Franke et al., 2023a; Jansen et al., 2024). Especially for Greenland, it has been shown in various  
dynamic ice regions that a three-dimensional representation aiming to depict deformation structures like folds accurately can  
contribute to understanding ice mechanical properties (Bons et al., 2016) and past flow patterns (Franke et al., 2022a; Jansen



et al., 2024). Notably, the profiles in the upstream region of the Jutulstraumen Ice Stream, as well as the region around EDML, where the high density of IRHs allows resolving small-scale englacial structures, and the profiles at the ice divides, have the potential to provide insights into past ice dynamics, such as ice flow direction changes or shifts in the location of ice divides.

## 5 Conclusions

We have mapped nine internal reflection horizons (IRHs) using radar data from various systems of the Alfred Wegener Institute, collected over the last three decades. Our IRHs cover the western DML, south of the Maud Belt, and range from 4.8 to 91.0 ka BP covering the Holocene and Last Glacial Period. Accurate dating of the IRHs was achieved by combining the age–depth chronology of the EPICA DML ice core and DEP-based radar forward modelling. Additionally, six of the new IRHs could be linked to deposits from significant historic bipolar volcanic eruptions, facilitating synchronization of these reflectors across Antarctica and potentially Greenland. Many of the IRHs mapped in this study likely correspond to the same englacial reflectors found in extensive regions over East and West Antarctica. A comparison with AWI EMR long-pulse data suggests that some of the IRHs identified here could be extended to even larger sectors of East Antarctica.

Our results significantly contribute to a broader understanding of the englacial age architecture of the DML Region in East Antarctica and highlight the potential for linking individual IRHs to other regions in Antarctica. Furthermore, the findings presented here are fundamental for enhancing our comprehension of past ice sheet processes and are crucial for numerical ice flow models aimed at improving our understanding of the paleoclimatic history of Antarctica.

*Data availability.* Our IRHs will be made publically available at PANGAEA upon publication. Reviewer access to the IRH data is provided via Nextcloud: <https://nextcloud.awi.de/s/DtYZCiiasxbxWHA>. The AICC2023, EDML ice core age–depth chronology (Bouchet et al., 2023) is available at PANGAEA: <https://doi.pangaea.de/10.1594/PANGAEA.961019>. Ice surface velocities from Mouginot et al. (2019) are available at the National Snow and Ice Data Center (NSIDC), <https://doi.org/10.7280/D10D4Z>. The drainage system boundaries Zwally et al. (2012) can be obtained here: <https://earth.gsfc.nasa.gov/cryo/data/polar-altimetry/antarctic-and-greenland-drainage-systems>. The BedMachine Antarctica V03 bed topography data from Morlighem et al. (2020) is available at <https://nsidc.org/data/nsidc-0756/versions/3>. The Reference Elevation Model of Antarctica (REMA) is available at the Polar Geospatial Centre: <https://www.pgc.umn.edu/data/rema/>.

## Appendix A: Crosspoint analysis

We performed an analysis of IRH depth differences at crossover points of intersecting radar lines to validate that we assigned the same reflections for the respective IRHs. For the analysis of crossover differences in the respective IRHs, we calculate the exact intersection points between the geometric lines formed by connecting the individual IRH picks. We create line subsets of one radar profile where IRH gaps exist to avoid creating lines, and therefore potential fake intersection points, where no IRHs are traced within a radar profile. Using these lines, we determine the location of the resulting intersection points. We then create a circular buffer around these intersection points and capture all IRH picks within this buffer. We select a buffer radius of 50 m



and average the IRH depths of all picks within a profile to minimize small-scale variations introduced by the semi-automatic  
440 tracker. The difference is derived from the mean depths of picks from both intersecting lines within the buffer.

Examining the histograms in Figure A2, we observe that most intersection point differences are below 10 meters depth  
difference, and the depth difference generally decreases for higher values. For the 4.8 ka and 7.2 ka IRHs, we see a small local  
maximum around a 5 m intersection point difference. Moreover, the differences become larger for older IRHs, leading to a  
higher number of larger crosspoint errors compared to younger IRHs.

#### 445 **Appendix B: Connection to Dome Fuji IRHs**

We can ascertain several points from a comparison of our IRHs with those from Wang et al. (2023), who traced IRHs around  
Dome Fuji using EMR long-pulse data. The IRHs from Wang et al. (2023) begin at greater depths relative to the surface,  
making them older relative to the IRHs in our study. However, the Dome Fuji region also allows tracing much older IRHs (up  
to 230 ka BP). Due to the availability of only EMR long-pulse data in this region, the range resolution is significantly coarser  
450 (approximately 50 m), resulting in a larger error in age dating compared to our IRHs. A direct comparison of two radargrams  
intersecting at Dome Fuji confirms that both the 36.3 ka and 75.3 ka IRHs from Wang et al. (2023) correspond to the same  
reflectors identified in our study, which we date as 38.1 ka and 73.4 ka, respectively (Figure B1). Additionally, it is likely that  
the reflection of the 135.6 ka IRH from Wang et al. (2023) corresponds to a reflection observed in the EMR short-pulse data  
(Figure B1).

#### 455 **Appendix C: IRH data set description**

We publish our dated IRHs on the *PANGAEA* Data Publisher (Felden et al., 2023) and comprises the information summarized  
in Table C1. It is important to note that the vertical position of the IRHs is provided in different formats: (1) as absolute two-  
way travel time (TWT) in the radargram, representing the direct reference to the radargram; (2) as TWT beneath our ice surface  
pick. To ensure this reference is clear for future users, we also provide the absolute TWT of the ice surface pick. For conversion  
460 between TWT to depth, we used a dielectric permittivity of  $\epsilon'_r = 3.15$  and a firn correction term of  $Z_{firn} = 13$  m (see Eq. 1).  
The IRH depth and elevation are referenced to the REMA surface DEM (version 2; Howat et al., 2019), relative to the WGS84  
ellipsoid. The Profile ID is the ID of the radargram, which also appears in the filename. The Paradigm ID is an internal AWI  
ID for referencing the AWI radar database and radar processing software where the picks are created and archived.

*Author contributions.* SF conceptualised the study, wrote the manuscript, traced and dated all IRHs, performed all data analysis, created all  
465 figures and validated the data. AMZ, DS and SF acquired radar data from the 2023/24 AWI MCoRDS campaign, while AMZ processed  
the data from this campaign with contributions of SF. AMZ, VH and SF contributed to tracing the ice-bed interface. JB provided context of  
comparable studies and for the discussion about connecting IRHs in this study over Antarctica. VH developed an algorithm for standard ice

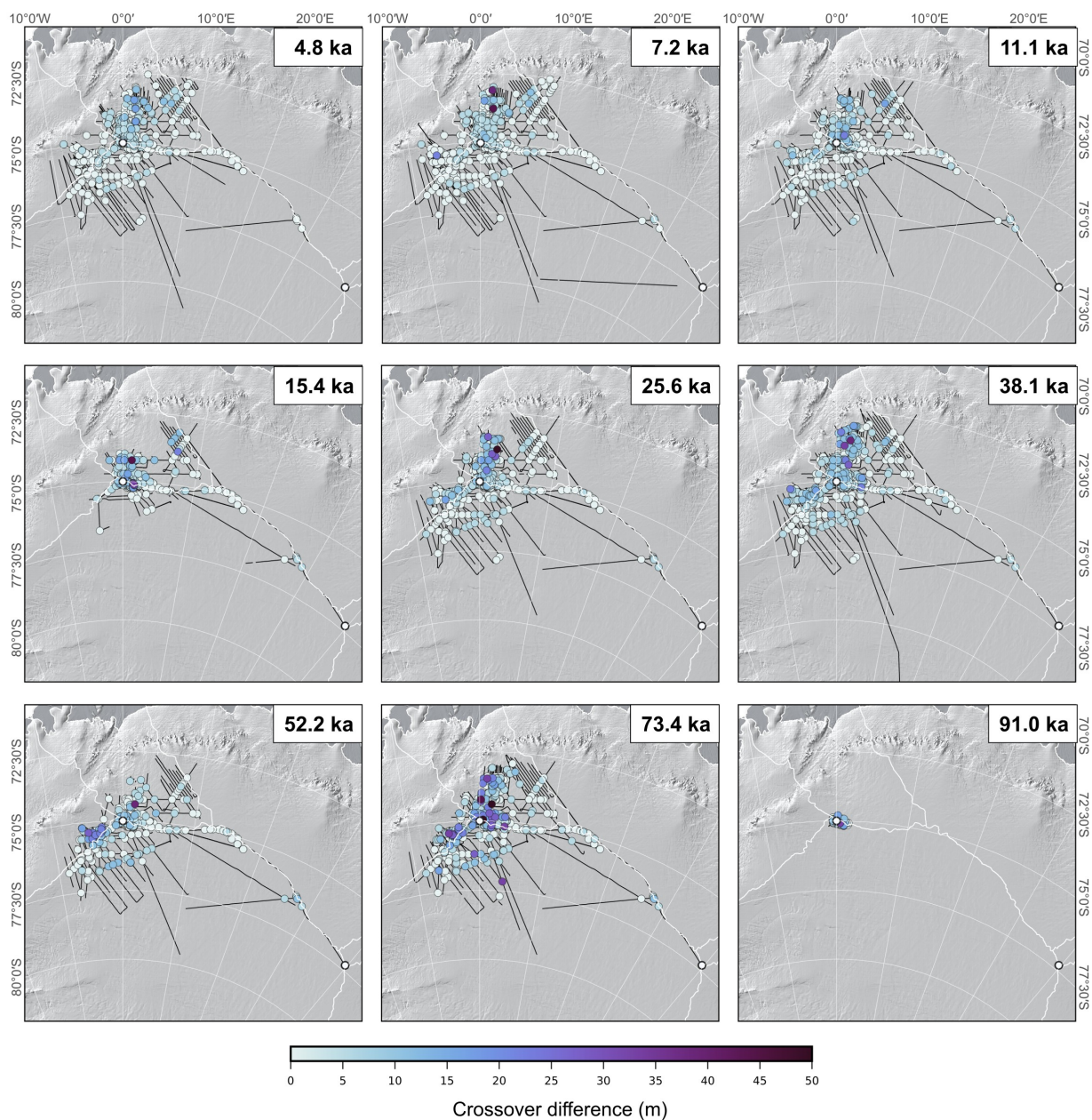


**Figure A1.** Differences of IRHs up to 50 m at crossing points.

surface tracking and processed GPS data. OE, DJ and VH implemented access and usability to AWI's radar data archive. All authors jointly revised and edited the manuscript.

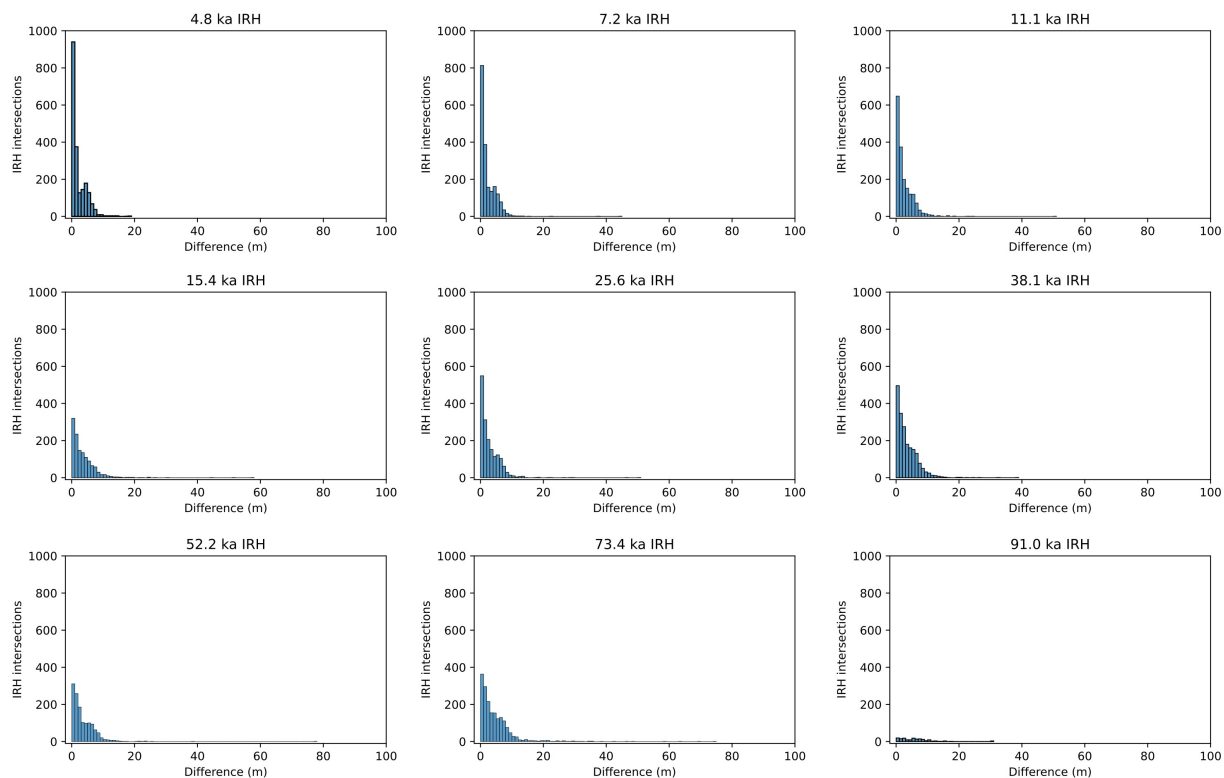


**Figure A2.** Histograms of the total count of differences of IRHs at crossing points up to 100 m. The bin width is 1 m.

470 *Competing interests.* The authors declare no competing interests.

*Acknowledgements.* We thank the AWI polar aircraft technicians Eduard Gebhard and Christoph Petersen for their support in the field during the 2023/24 radar campaign, the Kenn Borek crew of AWI's polar research aircrafts, as well as all supporters of previous radar campaigns mentioned in acknowledgements of related publications. Logistical support in the field over the past three decades has been provided by Neumayer III Station (Germany), Troll Station (Norway), Kohnen Station (Germany), Princess Elisabeth Station (Belgium),  
475 and Novolazarevskaya Airbase (Russia). We acknowledge the use of software from Open Polar Radar generated with support from the University of Kansas, NASA grants 80NSSC20K1242 and 80NSSC21K0753, and NSF grants OPP-2027615, OPP-2019719, OPP-1739003, IIS-1838230, RISE-2126503, RISE-2127606, and RISE-2126468. The authors would like to thank Aspen Technology, Inc. for providing software licenses and support. This study was motivated by the AntArchitecture Scientific Committee on Antarctic Research Action Group.

Steven Franke was funded by the Walter Benjamin Programme of the Deutsche Forschungsgemeinschaft (DFG, German Research Founda-  
480 tion; project number 506043073). Alexandra M. Zuhr was funded by the DFG in the framework of the priority program SPP 1158 "Antarctic Research with comparative investigations in Arctic ice areas" (grant number 522419679). Julien A. Bodart acknowledges funding from the Swiss National Science Foundation (grant number 211542).



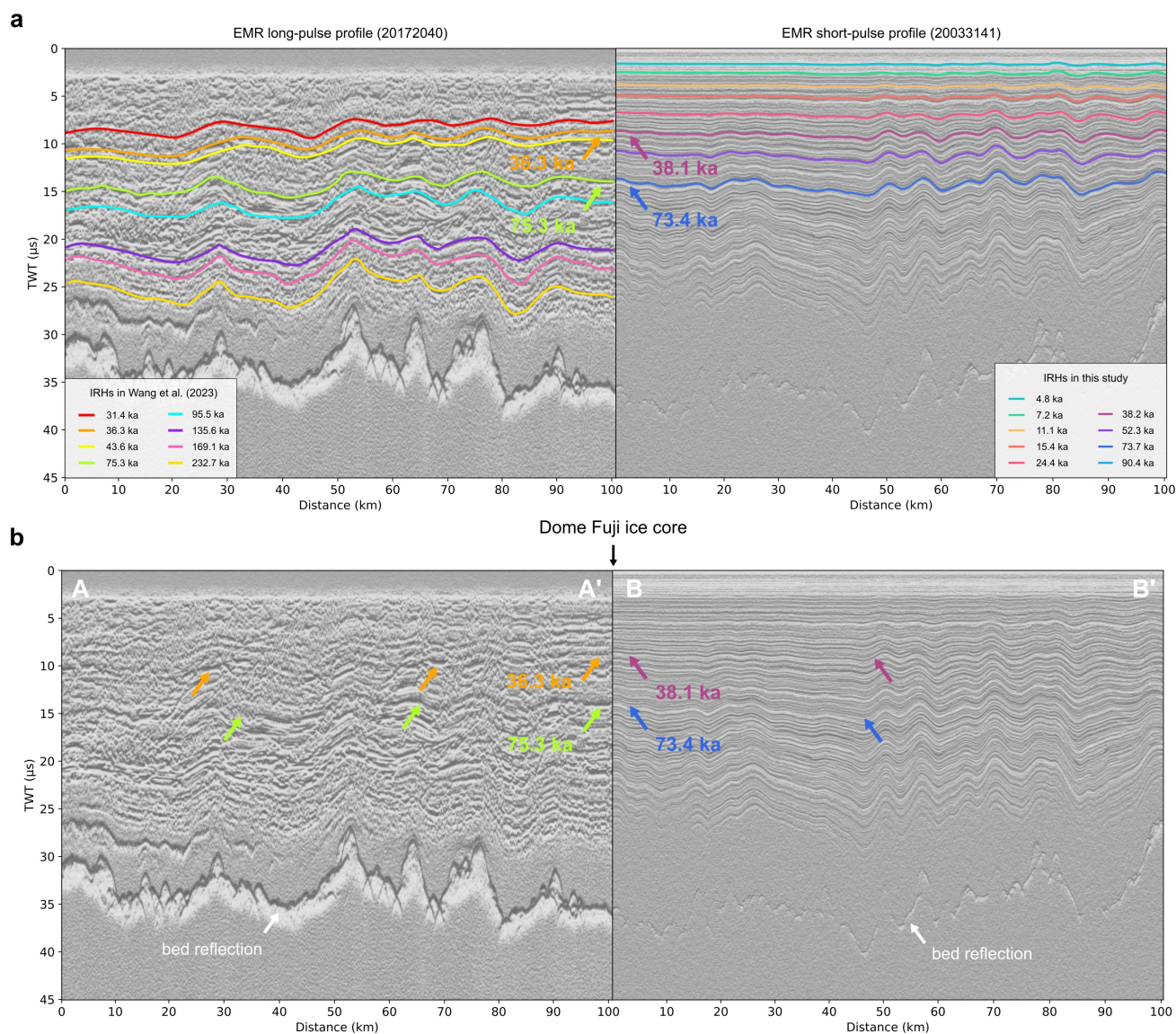


**Figure B1.** Illustration of two radargrams (AGC version) and the IRHs intersecting at the Dome Fuji ice core. Panel (a) shows the radargrams with IRHs, and panel (b) shows the radargrams without IRHs but where the Wang et al. (2023) IRHs intersect this study and Winter et al. (2019)'s IRHs at the Dome Fuji ice-core site. (a) The radargram on the left is an EMR long-pulse profile with IRHs from Wang et al. (2023), while the radargram on the right is an EMR short-pulse profile with IRHs from this study together with the IRHs from Winter et al. (2019). (b) The location at the Dome Fuji core, where the 36.3 ka and 75.3 ka IRH from Wang et al. (2023) intersects with the 38.1 ka and 73.4 ka IRH from this study and Winter et al. (2019) are marked with arrows. The colours of the IRHs in the left radargram correspond to those in Figure 2 in Wang et al. (2023). The location of the two profiles is shown in Figure 7 a.



**Table C1.** IRH data set description for column-separated text files.

Column name	Unit	Description
Profile ID		Radar profile ID
Paradigm ID		Radar Profile ID in the Paradigm system (AWI picking software)
Radar product		EMR short-pulse, MCoRDS narrowband, or MCoRDS wideband
Longitude	decimal degree	EPSG:4326
Latitude	decimal degree	EPSG:4326
IRH TWT	ns	absolute TWT in nanoseconds
IRH TWT ice	ns	TWT below ice surface in nanoseconds
Surface TWT	ns	TWT to ice surface in nanoseconds
Base TWT *	ns	TWT to ice base in nanoseconds
IRH depth	m	

\* The ice base reflection is not present in all radar profiles.

## References

- Alfred-Wegener-Institut Helmholtz-Zentrum für Polar- und Meeresforschung: Polar aircraft Polar5 and Polar6 operated by the Alfred Wegener Institute, *Journal of large-scale research facilities JLSRF*, 2, 87, <https://doi.org/10.17815/jlsrf-2-153>, 2016.
- Andersen, J., Newall, J., Blomdin, R., Sams, S., Fabel, D., Koester, A., Lifton, N., Fredin, O., Caffee, M., Glasser, N. F., Rogozhina, I., Suganuma, Y., Harbor, J., and Stroeven, A.: Ice surface changes during recent glacial cycles along the Jutulstraumen and Penck Trough ice streams in western Dronning Maud Land, East Antarctica, *Quaternary Science Reviews*, 249, 106 636, <https://doi.org/10.1016/j.quascirev.2020.106636>, 2020.
- Andersen, J. L., Newall, J. C., Fredin, O., Glasser, N. F., Lifton, N. A., Stuart, F. M., Fabel, D., Caffee, M., Pedersen, V. K., Koester, A. J., Suganuma, Y., Harbor, J. M., and Stroeven, A. P.: A topographic hinge-zone divides coastal and inland ice dynamic regimes in East Antarctica, *Communications Earth & Environment*, 4, 9, <https://doi.org/10.1038/s43247-022-00673-6>, 2023.
- Ashmore, D. W., Bingham, R. G., Ross, N., Siegert, M. J., Jordan, T. A., and Mair, D. W. F.: Englacial Architecture and Age-Depth Constraints Across the West Antarctic Ice Sheet, *Geophysical Research Letters*, 47, <https://doi.org/10.1029/2019gl086663>, 2020.
- Bazin, L., Landais, A., Lemieux-Dudon, B., Kele, H. T. M., Veres, D., Parrenin, F., Martinerie, P., Ritz, C., Capron, E., Lipenkov, V., Loutre, M.-F., Raynaud, D., Vinther, B., Svensson, A., Rasmussen, S. O., Severi, M., Blunier, T., Leuenberger, M., Fischer, H., Masson-Delmotte, V., Chappellaz, J., and Wolff, E.: An optimized multi-proxy, multi-site Antarctic ice and gas orbital chronology (AICC2012): 120&ndash;800 ka, *Climate of the Past*, 9, 1715–1731, <https://doi.org/10.5194/cp-9-1715-2013>, 2013.



- 500 Beem, L. H., Young, D. A., Greenbaum, J. S., Blankenship, D. D., Cavitte, M. G. P., Guo, J., and Bo, S.: Aerogeophysical characterization of Titan Dome, East Antarctica, and potential as an ice core target, *The Cryosphere*, 15, 1719–1730, <https://doi.org/10.5194/tc-15-1719-2021>, 2021.
- Bell, R. E., Ferraccioli, F., Creyts, T. T., Braaten, D., Corr, H., Das, I., Damaske, D., Frearson, N., Jordan, T., Rose, K., Studinger, M., and Wolovick, M.: Widespread Persistent Thickening of the East Antarctic Ice Sheet by Freezing from the Base, *Science*, 331, 1592–1595, <https://doi.org/10.1126/science.1200109>, 2011.
- 505 Bodart, J. A., Bingham, R. G., Ashmore, D. W., Karlsson, N. B., Hein, A. S., and Vaughan, D. G.: Age-Depth Stratigraphy of Pine Island Glacier Inferred From Airborne Radar and Ice-Core Chronology, *Journal of Geophysical Research: Earth Surface*, 126, <https://doi.org/10.1029/2020jf005927>, 2021.
- Bodart, J. A., Bingham, R. G., Young, D. A., MacGregor, J. A., Ashmore, D. W., Quartini, E., Hein, A. S., Vaughan, D. G., and Blankenship, D. D.: High mid-Holocene accumulation rates over West Antarctica inferred from a pervasive ice-penetrating radar reflector, *The*  
510 *Cryosphere*, 17, 1497–1512, <https://doi.org/10.5194/tc-17-1497-2023>, 2023.
- Bohleber, P., Wagner, N., and Eisen, O.: Permittivity of ice at radio frequencies: Part I. Coaxial transmission line cell, *Cold Regions Science and Technology*, 82, 56–67, <https://doi.org/10.1016/j.coldregions.2012.05.011>, 2012.
- Bons, P. D., Jansen, D., Mundel, F., Bauer, C. C., Binder, T., Eisen, O., Jessell, M. W., Llorens, M.-G., Steinbach, F., Steinhage, D., and Weikusat, I.: Converging flow and anisotropy cause large-scale folding in Greenland’s ice sheet, *Nature Communications*, 7, 11 427,  
515 <https://doi.org/10.1038/ncomms11427>, 2016.
- Bouchet, M., Landais, A., Grisart, A., Parrenin, F., Prié, F., Jacob, R., Fourré, E., Capron, E., Raynaud, D., Lipenkov, V. Y., Loutre, M.-F., Extier, T., Svensson, A. M., Martinerie, P., Leuenberger, M. C., Jiang, W., Ritterbusch, F., Lu, Z.-T., and Yang, G.-M.: AICC2023, EDML, PANGAEA, <https://doi.org/10.1594/PANGAEA.961019>, in: Bouchet, M et al. (2023): The Antarctic ice core chronology (AICC2023) [dataset bundled publication]. PANGAEA, <https://doi.org/10.1594/PANGAEA.961017>, 2023.
- 520 Bouchet, M., Landais, A., Grisart, A., Parrenin, F., Prié, F., Jacob, R., Fourré, E., Capron, E., Raynaud, D., Lipenkov, V. Y., Loutre, M.-F., Extier, T., Svensson, A., Legrain, E., Martinerie, P., Leuenberger, M., Jiang, W., Ritterbusch, F., Lu, Z.-T., and Yang, G.-M.: The Antarctic Ice Core Chronology 2023 (AICC2023) chronological framework and associated timescale for the European Project for Ice Coring in Antarctica (EPICA) Dome C ice core, *Climate of the Past*, 19, 2257–2286, <https://doi.org/10.5194/cp-19-2257-2023>, 2023.
- Braga, M. M. e., Jones, R. S., Bernales, J., Andersen, J. L., Fredin, O., Morlighem, M., Koester, A. J., Lifton, N. A., Harbor, J. M., Suganuma, Y., Glasser, N. F., Rogozhina, I., and Stroeven, A. P.: A thicker Antarctic ice stream during the mid-Pliocene warm period, *Communications Earth & Environment*, 4, 321, <https://doi.org/10.1038/s43247-023-00983-3>, 2023.
- 525 Carter, C. M., Bentley, M. J., Jamieson, S. S. R., Paxman, G. J. G., Jordan, T. A., Bodart, J. A., Ross, N., and Napoleoni, F.: Extensive palaeo-surfaces beneath the Evans–Rutford region of the West Antarctic Ice Sheet control modern and past ice flow, *The Cryosphere*, 18, 2277–2296, <https://doi.org/10.5194/tc-18-2277-2024>, 2024.
- 530 Cavitte, M. G. P., Blankenship, D. D., Young, D. A., Schroeder, D. M., Parrenin, F., Lemuer, E., MacGregor, J. A., and Siegert, M. J.: Deep radiostratigraphy of the East Antarctic plateau: connecting the Dome C and Vostok ice core sites, *Journal of Glaciology*, 62, 323–334, <https://doi.org/10.1017/jog.2016.11>, 2016.
- Cavitte, M. G. P., Parrenin, F., Ritz, C., Young, D. A., Lieffering, B. V., Blankenship, D. D., Frezzotti, M., and Roberts, J. L.: Accumulation patterns around Dome C, East Antarctica, in the last 73 kyr, *The Cryosphere*, 12, 1401–1414, <https://doi.org/10.5194/tc-12-1401-2018>,  
535 2018.



- Cavitte, M. G. P., Young, D. A., Mulvaney, R., Ritz, C., Greenbaum, J. S., Ng, G., Kempf, S. D., Quartini, E., Muldoon, G. R., Paden, J., Frezzotti, M., Roberts, J. L., Tozer, C. R., Schroeder, D. M., and Blankenship, D. D.: A detailed radiostratigraphic data set for the central East Antarctic Plateau spanning from the Holocene to the mid-Pleistocene, *Earth System Science Data*, 13, 4759–4777, <https://doi.org/10.5194/essd-13-4759-2021>, 2021.
- 540 Chesner, C. A.: The Toba Caldera Complex, *Quaternary International*, 258, 5–18, <https://doi.org/10.1016/j.quaint.2011.09.025>, 2012.
- Chung, A., Parrenin, F., Steinhage, D., Mulvaney, R., Martín, C., Cavitte, M. G. P., Lilien, D. A., Helm, V., Taylor, D., Gogineni, P., Ritz, C., Frezzotti, M., O’Neill, C., Miller, H., Dahl-Jensen, D., and Eisen, O.: Stagnant ice and age modelling in the Dome C region, Antarctica, *The Cryosphere*, 17, 3461–3483, <https://doi.org/10.5194/tc-17-3461-2023>, 2023.
- Drews, R., Eisen, O., Weikusat, I., Kipfstuhl, S., Lambrecht, A., Steinhage, D., Wilhelms, F., and Miller, H.: Layer disturbances and the  
545 radio-echo free zone in ice sheets, *The Cryosphere*, 3, 195–203, <https://doi.org/10.5194/tc-3-195-2009>, 2009.
- Drews, R., Schannwell, C., Ehlers, T. A., Gladstone, R., Pattyn, F., and Matsuoka, K.: Atmospheric and Oceanographic Signatures in the Ice Shelf Channel Morphology of Roi Baudouin Ice Shelf, East Antarctica, Inferred From Radar Data, *Journal of Geophysical Research: Earth Surface*, 125, <https://doi.org/10.1029/2020jf005587>, 2020.
- Dunbar, N. W., Iverson, N. A., Eaton, A. R. V., Sigl, M., Alloway, B. V., Kurbatov, A. V., Mastin, L. G., McConnell, J. R., and Wilson,  
550 C. J. N.: New Zealand supereruption provides time marker for the Last Glacial Maximum in Antarctica, *Scientific Reports*, 7, 12238, <https://doi.org/10.1038/s41598-017-11758-0>, 2017.
- Eisen, O., Wilhelms, F., Nixdorf, U., and Miller, H.: Revealing the nature of radar reflections in ice: DEP-based FDTD forward modeling, *Geophysical Research Letters*, 30, <https://doi.org/10.1029/2002gl016403>, 2003.
- Eisen, O., Rack, W., Nixdorf, U., and Wilhelms, F.: Characteristics of accumulation around the EPICA deep-drilling site in Dronning Maud  
555 Land, Antarctica, *Annals of Glaciology*, 41, 41–46, <https://doi.org/10.3189/172756405781813276>, 2005.
- Eisen, O., Wilhelms, F., Steinhage, D., and Schwander, J.: Improved method to determine radio-echo sounding reflector depths from ice-core profiles of permittivity and conductivity, *Journal of Glaciology*, 52, 299–310, <https://doi.org/10.3189/172756506781828674>, 2006.
- Eisen, O., Hamann, I., Kipfstuhl, S., Steinhage, D., and Wilhelms, F.: Direct evidence for continuous radar reflector originating from changes in crystal-orientation fabric, *The Cryosphere*, 1, 1–10, <https://doi.org/10.5194/tc-1-1-2007>, 2007.
- 560 Eisermann, H., Eagles, G., Ruppel, A., Smith, E. C., and Jokat, W.: Bathymetry Beneath Ice Shelves of Western Dronning Maud Land, East Antarctica, and Implications on Ice Shelf Stability, *Geophysical Research Letters*, 47, <https://doi.org/10.1029/2019gl086724>, 2020.
- Felden, J., Möller, L., Schindler, U., Huber, R., Schumacher, S., Koppe, R., Diepenbroek, M., and Glöckner, F. O.: PANGAEA - Data Publisher for Earth & Environmental Science, *Scientific Data*, 10, 347, <https://doi.org/10.1038/s41597-023-02269-x>, 2023.
- Franke, S., Eisermann, H., Jokat, W., Eagles, G., Asseng, J., Miller, H., Steinhage, D., Helm, V., Eisen, O., and Jansen, D.: Preserved  
565 landscapes underneath the Antarctic Ice Sheet reveal the geomorphological history of Jutulstraumen Basin, *Earth Surface Processes and Landforms*, 46, 2728–2745, <https://doi.org/10.1002/esp.5203>, 2021.
- Franke, S., Bons, P. D., Westhoff, J., Weikusat, I., Binder, T., Streng, K., Steinhage, D., Helm, V., Eisen, O., Paden, J. D., Eagles, G., and Jansen, D.: Holocene ice-stream shutdown and drainage basin reconfiguration in northeast Greenland, *Nature Geoscience*, 15, 995–1001, <https://doi.org/10.1038/s41561-022-01082-2>, 2022a.
- 570 Franke, S., Jansen, D., Binder, T., Paden, J. D., Dörr, N., Gerber, T. A., Miller, H., Dahl-Jensen, D., Helm, V., Steinhage, D., Weikusat, I., Wilhelms, F., and Eisen, O.: Airborne ultra-wideband radar sounding over the shear margins and along flow lines at the onset region of the Northeast Greenland Ice Stream, *Earth System Science Data*, 14, 763–779, <https://doi.org/10.5194/essd-14-763-2022>, 2022b.





- 575 Franke, S., Bons, P. D., Streng, K., Mundel, F., Binder, T., Weikusat, I., Bauer, C. C., Paden, J. D., Dörr, N., Helm, V., Steinhage, D., Eisen, O., and Jansen, D.: Three-dimensional topology dataset of folded radar stratigraphy in northern Greenland, *Scientific Data*, 10, 525, <https://doi.org/10.1038/s41597-023-02339-0>, 2023a.
- Franke, S., Gerber, T., Warren, C., Jansen, D., Eisen, O., and Dahl-Jensen, D.: Investigating the Radar Response of Englacial Debris Entrained Basal Ice Units in East Antarctica Using Electromagnetic Forward Modeling, *IEEE Transactions on Geoscience and Remote Sensing*, 61, 1–16, <https://doi.org/10.1109/tgrs.2023.3277874>, 2023b.
- 580 Franke, S., Wolovick, M., Drews, R., Jansen, D., Matsuoka, K., and Bons, P. D.: Sediment Freeze-On and Transport Near the Onset of a Fast-Flowing Glacier in East Antarctica, *Geophysical Research Letters*, 51, <https://doi.org/10.1029/2023gl107164>, 2024.
- Fretwell, P., Pritchard, H. D., Vaughan, D. G., Bamber, J. L., Barrand, N. E., Bell, R., Bianchi, C., Bingham, R. G., Blankenship, D. D., Casassa, G., Catania, G., Callens, D., Conway, H., Cook, A. J., Corr, H. F. J., Damaske, D., Damm, V., Ferraccioli, F., Forsberg, R., Fujita, S., Gim, Y., Gogineni, P., Griggs, J. A., Hindmarsh, R. C. A., Holmlund, P., Holt, J. W., Jacobel, R. W., Jenkins, A., Jokat, W., Jordan, T., King, E. C., Kohler, J., Krabill, W., Riger-Kusk, M., Langley, K. A., Leitchenkov, G., Leuschen, C., Luyendyk, B. P., Matsuoka, K., 585 Mouginit, J., Nitsche, F. O., Nogi, Y., Nost, O. A., Popov, S. V., Rignot, E., Rippin, D. M., Rivera, A., Roberts, J., Ross, N., Siegert, M. J., Smith, A. M., Steinhage, D., Studinger, M., Sun, B., Tinto, B. K., Welch, B. C., Wilson, D., Young, D. A., Xiangbin, C., and Zirizzotti, A.: Bedmap2: improved ice bed, surface and thickness datasets for Antarctica, *The Cryosphere*, 7, 375–393, <https://doi.org/10.5194/tc-7-375-2013>, 2013.
- Frémand, A. C., Bodart, J. A., Jordan, T. A., Ferraccioli, F., Robinson, C., Corr, H. F. J., Peat, H. J., Bingham, R. G., and Vaughan, D. G.: 590 British Antarctic Survey’s aerogeophysical data: releasing 25 years of airborne gravity, magnetic, and radar datasets over Antarctica, *Earth System Science Data*, 14, 3379–3410, <https://doi.org/10.5194/essd-14-3379-2022>, 2022.
- Fudge, T. J., Hills, B. H., Horlings, A. N., Holschuh, N., Christian, J. E., Davidge, L., Hoffman, A., O’Connor, G. K., Christianson, K., and Steig, E. J.: A site for deep ice coring at West Hercules Dome: results from ground-based geophysics and modeling, *Journal of Glaciology*, 69, 538–550, <https://doi.org/10.1017/jog.2022.80>, 2023.
- 595 Fujita, S., Maeno, H., Uratsuka, S., Furukawa, T., Mae, S., Fujii, Y., and Watanabe, O.: Nature of radio echo layering in the Antarctic Ice Sheet detected by a two-frequency experiment, *Journal of Geophysical Research: Solid Earth*, 104, 13 013–13 024, <https://doi.org/10.1029/1999jb900034>, 1999.
- Giannopoulos, A.: Modelling ground penetrating radar by GprMax, *Construction and Building Materials*, 19, 755–762, <https://doi.org/10.1016/j.conbuildmat.2005.06.007>, 2005.
- 600 Giannopoulos, A.: Unsplit Implementation of Higher Order PMLs, *IEEE Transactions on Antennas and Propagation*, 60, 1479–1485, <https://doi.org/10.1109/TAP.2011.2180344>, 2012.
- Glen, J. W. and Paren, J. G.: The Electrical Properties of Snow and Ice, *Journal of Glaciology*, 15, 15–38, <https://doi.org/10.3189/s0022143000034249>, 1975.
- Hale, R., Miller, H., Gogineni, S., Yan, J. B., Rodriguez-Morales, F., Leuschen, C., Paden, J., Li, J., Binder, T., Steinhage, D., Gehrman, M., 605 and Braaten, D.: Multi-Channel Ultra-Wideband Radar Sounder and Imager, 2016 IEEE International Geoscience and Remote Sensing Symposium (IGARSS), pp. 2112–2115, <https://doi.org/10.1109/igarss.2016.7729545>, 2016.
- Hammer, C. U.: Acidity of Polar Ice Cores in Relation to Absolute Dating, Past Volcanism, and Radio-Echoes, *Journal of Glaciology*, 25, 359–372, <https://doi.org/10.3189/s0022143000015227>, 1980.
- Harrison, C. H.: Radio Echo Sounding of Horizontal Layers in Ice, *Journal of Glaciology*, 12, 383–397, 610 <https://doi.org/10.3189/s0022143000031804>, 1973.



- Holschuh, N., Christianson, K., and Anandakrishnan, S.: Power loss in dipping internal reflectors, imaged using ice-penetrating radar, *Annals of Glaciology*, 55, 49–56, <https://doi.org/10.3189/2014aog67a005>, 2014.
- Howat, I. M., Porter, C., Smith, B. E., Noh, M.-J., and Morin, P.: The Reference Elevation Model of Antarctica, *The Cryosphere*, 13, 665–674, <https://doi.org/10.5194/tc-13-665-2019>, 2019.
- 615 Huybrechts, P., Rybak, O., Steinhage, D., and Pattyn, F.: Past and present accumulation rate reconstruction along the Dome Fuji–Kohnen radio-echo sounding profile, Dronning Maud Land, East Antarctica, *Annals of Glaciology*, 50, 112–120, <https://doi.org/10.3189/172756409789097513>, 2009.
- IPCC: Ocean, Cryosphere and Sea Level Change, p. 1211–1362, Cambridge University Press, <https://doi.org/10.1017/9781009157896.011>, 2023.
- 620 Jacobel, R. W. and Welch, B. C.: A time marker at 17.5 kyr BP detected throughout West Antarctica, *Annals of Glaciology*, 41, 47–51, <https://doi.org/10.3189/172756405781813348>, 2005.
- Jansen, D., Franke, S., Bauer, C. C., Binder, T., Dahl-Jensen, D., Eichler, J., Eisen, O., Hu, Y., Kerch, J., Llorens, M.-G., Miller, H., Neckel, N., Paden, J., Riese, T. d., Sachau, T., Stoll, N., Weikusat, I., Wilhelms, F., Zhang, Y., and Bons, P. D.: Shear margins in upper half of Northeast Greenland Ice Stream were established two millennia ago, *Nature Communications*, 15, 1193, <https://doi.org/10.1038/s41467-024-45021-8>, 2024.
- 625 Karlsson, N. B., Dahl-Jensen, D., Gogineni, S. P., and Paden, J. D.: Tracing the depth of the Holocene ice in North Greenland from radio-echo sounding data, *Annals of Glaciology*, 54, 44–50, <https://doi.org/10.3189/2013aog64a057>, 2013.
- Karlsson, N. B., Binder, T., Eagles, G., Helm, V., Pattyn, F., Lieffering, B. V., and Eisen, O.: Glaciological characteristics in the Dome Fuji region and new assessment for “Oldest Ice”, *The Cryosphere*, 12, 2413–2424, <https://doi.org/10.5194/tc-12-2413-2018>, 2018.
- 630 Kjær, K. H., Larsen, N. K., Binder, T., Bjørk, A. A., Eisen, O., Fahnestock, M. A., Funder, S., Garde, A. A., Haack, H., Helm, V., Houmark-Nielsen, M., Kjeldsen, K. K., Khan, S. A., Machguth, H., McDonald, I., Morlighem, M., Mouginot, J., Paden, J. D., Waight, T. E., Weikusat, C., Willerslev, E., and MacGregor, J. A.: A large impact crater beneath Hiawatha Glacier in northwest Greenland, *Science Advances*, 4, eaar8173, <https://doi.org/10.1126/sciadv.aar8173>, 2018.
- Koch, I., Drews, R., Franke, S., Jansen, D., Oraschewski, F. M., Muhle, L. S., Višnjević, V., Matsuoka, K., Pattyn, F., and Eisen, O.: Radar 635 internal reflection horizons from multisystem data reflect ice dynamic and surface accumulation history along the Princess Ragnhild Coast, Dronning Maud Land, East Antarctica, *Journal of Glaciology*, pp. 1–19, <https://doi.org/10.1017/jog.2023.93>, 2023.
- Leysinger Vieli, G. J. C., Hindmarsh, R. C. A., Siegert, M. J., and Bo, S.: Time-dependence of the spatial pattern of accumulation rate in East Antarctica deduced from isochronic radar layers using a 3-D numerical ice flow model, *Journal of Geophysical Research: Earth Surface*, 116, <https://doi.org/10.1029/2010jf001785>, 2011.
- 640 Leysinger Vieli, G. J.-M. C., Siegert, M. J., and Payne, A. J.: Reconstructing ice-sheet accumulation rates at ridge B, East Antarctica, *Annals of Glaciology*, 39, 326–330, <https://doi.org/10.3189/172756404781814519>, 2004.
- Leysinger Vieli, G. J.-M. C., Martín, C., Hindmarsh, R. C. A., and Lüthi, M. P.: Basal freeze-on generates complex ice-sheet stratigraphy, *Nature Communications*, 9, 4669, <https://doi.org/10.1038/s41467-018-07083-3>, 2018.
- 645 Lin, J., Svensson, A., Hvidberg, C. S., Lohmann, J., Kristiansen, S., Dahl-Jensen, D., Steffensen, J. P., Rasmussen, S. O., Cook, E., Kjær, H. A., Vinther, B. M., Fischer, H., Stocker, T., Sigl, M., Bigler, M., Severi, M., Traversi, R., and Mulvaney, R.: Magnitude, frequency and climate forcing of global volcanism during the last glacial period as seen in Greenland and Antarctic ice cores (60–9ka), *Climate of the Past*, 18, 485–506, <https://doi.org/10.5194/cp-18-485-2022>, 2022.



- Lin, J., Abbott, P. M., Sigl, M., Steffensen, J. P., Mulvaney, R., Severi, M., and Svensson, A.: Bipolar ice-core records constrain possible dates and global radiative forcing following the ~74 ka Toba eruption, *Quaternary Science Reviews*, 312, 108–162, <https://doi.org/10.1016/j.quascirev.2023.108162>, 2023.
- Lythe, M. B. and Vaughan, D. G.: BEDMAP: A new ice thickness and subglacial topographic model of Antarctica, *Journal of Geophysical Research: Solid Earth*, 106, 11 335–11 351, <https://doi.org/10.1029/2000jb900449>, 2001.
- MacGregor, J. A., Fahnestock, M. A., Catania, G. A., Paden, J. D., Gogineni, S. P., Young, S. K., Rybarski, S. C., Mabrey, A. N., Wagman, B. M., and Morlighem, M.: Radiostratigraphy and age structure of the Greenland Ice Sheet, *Journal of Geophysical Research: Earth Surface*, 120, 212–241, <https://doi.org/10.1002/2014jf003215>, 2015.
- Millar, D. H. M.: Radio-echo layering in polar ice sheets and past volcanic activity, *Nature*, 292, 441–443, <https://doi.org/10.1038/292441a0>, 1981.
- Mojtabavi, S., Eisen, O., Franke, S., Jansen, D., Steinhage, D., Paden, J., Dahl-Jensen, D., Weikusat, I., Eichler, J., and Wilhelms, F.: Origin of englacial stratigraphy at three deep ice core sites of the Greenland Ice Sheet by synthetic radar modelling, *Journal of Glaciology*, 68, 799–811, <https://doi.org/10.1017/jog.2021.137>, 2022.
- Moore, J. C.: High-resolution dielectric profiling of ice cores, *Journal of Glaciology*, 39, 245–248, <https://doi.org/10.3189/s0022143000015902>, 1993.
- Moqadam, H. and Eisen, O.: Review article: Feature tracing in radio-echo sounding products of terrestrial ice sheets and planetary bodies, *The Cryosphere Discussions [preprint]*, 2024, 1–58, <https://doi.org/10.5194/egusphere-2024-1674>, 2024.
- Morlighem, M., Rignot, E., Binder, T., Blankenship, D., Drews, R., Eagles, G., Eisen, O., Ferraccioli, F., Forsberg, R., Fretwell, P., Goel, V., Greenbaum, J. S., Gudmundsson, H., Guo, J., Helm, V., Hofstede, C., Howat, I., Humbert, A., Jokat, W., Karlsson, N. B., Lee, W. S., Matsuoka, K., Millan, R., Mouginit, J., Paden, J., Pattyn, F., Roberts, J., Rosier, S., Ruppel, A., Seroussi, H., Smith, E. C., Steinhage, D., Sun, B., Broeke, M. R. v. d., Ommen, T. D. v., Wessem, M. v., and Young, D. A.: Deep glacial troughs and stabilizing ridges unveiled beneath the margins of the Antarctic ice sheet, *Nature Geoscience*, 13, 132–137, <https://doi.org/10.1038/s41561-019-0510-8>, 2020.
- Mouginit, J., Rignot, E., and Scheuchl, B.: Continent-Wide, Interferometric SAR Phase, Mapping of Antarctic Ice Velocity, *Geophysical Research Letters*, 46, 9710–9718, <https://doi.org/10.1029/2019gl083826>, 2019.
- Muldoon, G. R., Jackson, C. S., Young, D. A., and Blankenship, D. D.: Bayesian estimation of englacial radar chronology in Central West Antarctica, *Dynamics and Statistics of the Climate System*, 3, dzy004, <https://doi.org/10.1093/climatesystem/dzy004>, 2018.
- Nixdorf, U., Steinhage, D., Meyer, U., Hempel, L., Jenett, M., Wachs, P., and Miller, H.: The newly developed airborne radio-echo sounding system of the AWI as a glaciological tool, *Annals of Glaciology*, 29, 231–238, <https://doi.org/10.3189/172756499781821346>, 1999.
- Näslund, J.: Subglacial Preservation of Valley Morphology at Amundsenisen, Western Dronning Maud Land, Antarctica, *Earth Surface Processes and Landforms*, 22, 441–455, [https://doi.org/10.1002/\(sici\)1096-9837\(199705\)22:5<441::aid-esp696>3.0.co;2-4](https://doi.org/10.1002/(sici)1096-9837(199705)22:5<441::aid-esp696>3.0.co;2-4), 1997.
- Open Polar Radar: Open Polar Radar. opr (Version 3.0.1) [Computer software], <https://doi.org/10.5281/zenodo.5683959>, 2023.
- Oyabu, I., Kawamura, K., Fujita, S., Inoue, R., Motoyama, H., Fukui, K., Hirabayashi, M., Hoshina, Y., Kurita, N., Nakazawa, F., Ohno, H., Sugiura, K., Suzuki, T., Tsutaki, S., Abe-Ouchi, A., Niwano, M., Parrenin, F., Saito, F., and Yoshimori, M.: Temporal variations of surface mass balance over the last 5000 years around Dome Fuji, Dronning Maud Land, East Antarctica, *Climate of the Past*, 19, 293–321, <https://doi.org/10.5194/cp-19-293-2023>, 2023.
- Panton, C. and Karlsson, N. B.: Automated mapping of near bed radio-echo layer disruptions in the Greenland Ice Sheet, *Earth and Planetary Science Letters*, 432, 323–331, <https://doi.org/10.1016/j.epsl.2015.10.024>, 2015.



- 685 Paren, J. G. and Robin, G. d. Q.: Internal Reflections in Polar Ice Sheets, *Journal of Glaciology*, 14, 251–259, <https://doi.org/10.3189/s0022143000021730>, 1975.
- Riedel, S., Jokat, W., and Steinhage, D.: Mapping tectonic provinces with airborne gravity and radar data in Dronning Maud Land, East Antarctica, *Geophysical Journal International*, 189, 414–427, <https://doi.org/10.1111/j.1365-246x.2012.05363.x>, 2012.
- Rippin, D. M., Bamber, J. L., Siegert, M. J., Vaughan, D. G., and Corr, H. F. J.: Basal topography and ice flow in the Bailey/Slessor region  
690 of East Antarctica, *Journal of Geophysical Research: Earth Surface*, 108, <https://doi.org/10.1029/2003jf000039>, 2003.
- Rippin, D. M., Siegert, M. J., Bamber, J. L., Vaughan, D. G., and Corr, H. F. J.: Switch-off of a major enhanced ice flow unit in East Antarctica, *Geophysical Research Letters*, 33, <https://doi.org/10.1029/2006gl026648>, 2006.
- Robin, G. D. Q., Evans, S., and Bailey, J. T.: Interpretation of radio echo sounding in polar ice sheets, *Philosophical Transactions of the Royal Society of London. Series A, Mathematical and Physical Sciences*, 265, 437–505, <https://doi.org/10.1098/rsta.1969.0063>, 1969.
- 695 Robin, G. D. Q., Drewry, D. J., and Meldrum, D. T.: International studies of ice sheet and bedrock, *Philosophical Transactions of the Royal Society of London. B, Biological Sciences*, 279, 185–196, <https://doi.org/10.1098/rstb.1977.0081>, 1977.
- Rodriguez-Morales, F., Byers, K., Crowe, R., Player, K., Hale, R. D., Arnold, E. J., Smith, L., Gifford, C. M., Braaten, D., Panton, C., Gogineni, S., Leuschen, C. J., Paden, J. D., Li, J., Lewis, C. C., Panzer, B., Alvestegui, D. G.-G., and Patel, A.: Advanced Multifrequency Radar Instrumentation for Polar Research, *IEEE Transactions on Geoscience and Remote Sensing*, 52, 2824–2842,  
700 <https://doi.org/10.1109/tgrs.2013.2266415>, 2013.
- Rose, K. C., Ross, N., Jordan, T. A., Bingham, R. G., Corr, H. F. J., Ferraccioli, F., Brocq, A. M. L., Rippin, D. M., and Siegert, M. J.: Ancient pre-glacial erosion surfaces preserved beneath the West Antarctic Ice Sheet, *Earth Surface Dynamics*, 3, 139–152, <https://doi.org/10.5194/esurf-3-139-2015>, 2015.
- Rotschky, G., Holmlund, P., Isaksson, E., Mulvaney, R., Oerter, H., Broeke, M. R. V. D., and Winther, J.-G.: A new surface accumulation map for western Dronning Maud Land, Antarctica, from interpolation of point measurements, *Journal of Glaciology*, 53, 385–398,  
705 <https://doi.org/10.3189/002214307783258459>, 2007.
- Sanderson, R. J., Winter, K., Callard, S. L., Napoleoni, F., Ross, N., Jordan, T. A., and Bingham, R. G.: Englacial architecture of Lambert Glacier, East Antarctica, *The Cryosphere*, 17, 4853–4871, <https://doi.org/10.5194/tc-17-4853-2023>, 2023.
- Santin, I., Roncoroni, G., Forte, E., Gutgesell, P., and Pipan, M.: GPR modelling and inversion to quantify the debris content within ice, *Near  
710 Surface Geophysics*, <https://doi.org/10.1002/nsg.12274>, 2023.
- Siegert, M. J., Welch, B., Morse, D., Vieli, A., Blankenship, D. D., Joughin, I., King, E. C., Vieli, G. J.-M. C. L., Payne, A. J., and Jacobel, R.: Ice Flow Direction Change in Interior West Antarctica, *Science*, 305, 1948–1951, <https://doi.org/10.1126/science.1101072>, 2004.
- Siegert, M. J., Pokar, M., Dowdeswell, J. A., and Benham, T.: Radio-echo layering in West Antarctica: a spreadsheet dataset, *Earth Surface Processes and Landforms*, 30, 1583–1591, <https://doi.org/10.1002/esp.1238>, 2005.
- 715 Steinhage, D.: Beitrage aus geophysikalischen Messungen in Dronning Maud Land, Antarktis, zur Auffindung eines optimalen Bohrpunktes für eine Eiskerntiefbohrung, *Berichte zur Polar und Meeresforschung*, 2001.
- Steinhage, D., Nixdorf, U., Meyer, U., and Miller, H.: Subglacial topography and internal structure of central and western Dronning Maud Land, Antarctica, determined from airborne radio echo sounding, *Journal of Applied Geophysics*, 47, 183–189, [https://doi.org/10.1016/s0926-9851\(01\)00063-5](https://doi.org/10.1016/s0926-9851(01)00063-5), 2001.
- 720 Steinhage, D., Kipfstuhl, S., Nixdorf, U., and Miller, H.: Internal structure of the ice sheet between Kohonen station and Dome Fuji, Antarctica, revealed by airborne radio-echo sounding, *Annals of Glaciology*, 54, 163–167, <https://doi.org/10.3189/2013aog64a113>, 2013.





- Sutter, J., Fischer, H., and Eisen, O.: Investigating the internal structure of the Antarctic ice sheet: the utility of isochrones for spatiotemporal ice-sheet model calibration, *The Cryosphere*, 15, 3839–3860, <https://doi.org/10.5194/tc-15-3839-2021>, 2021.
- 725 Svensson, A., Bigler, M., Blunier, T., Clausen, H. B., Dahl-Jensen, D., Fischer, H., Fujita, S., Goto-Azuma, K., Johnsen, S. J., Kawamura, K., Kipfstuhl, S., Kohno, M., Parrenin, F., Popp, T., Rasmussen, S. O., Schwander, J., Seierstad, I., Severi, M., Steffensen, J. P., Udisti, R., Uemura, R., Vallelonga, P., Vinther, B. M., Wegner, A., Wilhelms, F., and Winstrup, M.: Direct linking of Greenland and Antarctic ice cores at the Toba eruption (74 ka BP), *Climate of the Past*, 9, 749–766, <https://doi.org/10.5194/cp-9-749-2013>, 2013.
- Taflove, A. and Hagness, S. C.: *Computational electrodynamics: the finite-difference time-domain method*, Artech House, 3rd edn., 2005.
- 730 Višnjević, V., Drews, R., Schannwell, C., Koch, I., Franke, S., Jansen, D., and Eisen, O.: Predicting the steady-state isochronal stratigraphy of ice shelves using observations and modeling, *The Cryosphere*, 16, 4763–4777, <https://doi.org/10.5194/tc-16-4763-2022>, 2022.
- Wang, Z., Chung, A., Steinhage, D., Parrenin, F., Freitag, J., and Eisen, O.: Mapping age and basal conditions of ice in the Dome Fuji region, Antarctica, by combining radar internal layer stratigraphy and flow modeling, *The Cryosphere*, 17, 4297–4314, <https://doi.org/10.5194/tc-17-4297-2023>, 2023.
- 735 Warren, C., Giannopoulos, A., and Giannakis, I.: gprMax: Open source software to simulate electromagnetic wave propagation for Ground Penetrating Radar, *Computer Physics Communications*, 209, 163–170, <https://doi.org/10.1016/j.cpc.2016.08.020>, 2016.
- Wilhelms, F., Kipfstuhl, J., Miller, H., Heinloth, K., and Firestone, J.: Precise dielectric profiling of ice cores: a new device with improved guarding and its theory, *Journal of Glaciology*, 44, 171–174, <https://doi.org/10.3189/s002214300000246x>, 1998.
- 740 Winter, A., Steinhage, D., Arnold, E. J., Blankenship, D. D., Cavitte, M. G. P., Corr, H. F. J., Paden, J. D., Urbini, S., Young, D. A., and Eisen, O.: Comparison of measurements from different radio-echo sounding systems and synchronization with the ice core at Dome C, Antarctica, *The Cryosphere*, 11, 653–668, <https://doi.org/10.5194/tc-11-653-2017>, 2017.
- Winter, A., Steinhage, D., Creyts, T. T., Kleiner, T., and Eisen, O.: Age stratigraphy in the East Antarctic Ice Sheet inferred from radio-echo sounding horizons, *Earth System Science Data*, 11, 1069–1081, <https://doi.org/10.5194/essd-11-1069-2019>, 2019.
- Yee, K.: Numerical solution of initial boundary value problems involving maxwell's equations in isotropic media, *IEEE Transactions on Antennas and Propagation*, 14, 302–307, <https://doi.org/10.1109/TAP.1966.1138693>, 1966.
- 745 Zwally, H. J., Giovinetto, M. B., Beckley, M. A., and Saba, J. L.: Antarctic and Greenland drainage systems, GSFC cryospheric sciences laboratory, [http://icesat4.gsfc.nasa.gov/cryo\\_data/ant\\_grn\\_drainage\\_systems.php](http://icesat4.gsfc.nasa.gov/cryo_data/ant_grn_drainage_systems.php), 2012.